Transition and Electron Impact Excitation Collision Rates for OIII

S. S. Tayal¹ and O. Zatsarinny²

Department of Physics, Clark Atlanta University, Atlanta, GA 30314, Georgia; stayal@cau.edu
 Department of Physics and Astronomy, Drake University, Des Moines, IA 50311, USA; oleg.zatsarinny@drake.edu
 Received 2017 August 17; revised 2017 October 13; accepted 2017 October 15; published 2017 November 28

Abstract

Transition probabilities, electron excitation collision strengths, and rate coefficients for a large number of O III lines over a broad wavelength range, from the infrared to ultraviolet, have been reported. The collision strengths have been calculated in the close-coupling approximation using the B-spline Breit–Pauli *R*-matrix method. The multiconfiguration Hartree–Fock method in combination with B-spline expansions is employed for an accurate representation of the target wave functions. The close-coupling expansion contains 202 O^{2+} fine-structure levels of the $2s^22p^2$, $2s2p^3$, $2p^4$, $2s^22p3s$, 3p, 3d, 4s, 4p, 4d, 4f, 5s, and $2s2p^33s$, 3p, 3d configurations. The effective collision strengths are obtained by averaging electron excitation collision strengths over a Maxwellian distribution of velocities at electron temperatures ranging from 100 to 100,000 K. The calculated effective collision strengths have been reported for the 20,302 transitions between all 202 fine-structure levels. There is an overall good agreement with the recent *R*-matrix calculations by Storey et al. for the transitions between all levels of the ground $2s^22p^2$ configuration, but significant discrepancies have been found with Palay et al. for transitions to the $2s^22p^2$ $1s_0$ level. Line intensity ratios between the optical lines arising from the $2s^22p^2$ $3p_{0,1,2}$ $1s_0$ transitions have been compared with other calculations and observations from the photoionized gaseous nebulae, and good agreement is found. The present calculations provide the most complete and accurate data sets, which should allow a more detailed treatment of the available measured spectra from different ground and space observatories.

Key words: atomic data – atomic processes – H II regions – line: formation – scattering *Supporting material:* machine-readable tables

1. Introduction

Accurate transition rates and electron collision excitation rates of O²⁺ are important for the analysis and diagnostics of a wide range of spectra from various types of astrophysical objects. A number of O III bright spectral features have been observed in a broad wavelength region from the infrared to ultraviolet. The O III lines provide important diagnostic tools to determine the oxygen abundance and other physical conditions in the Milky Way and Seyfert galaxies (Maiolino et al. 2008). Planetary nebulae and H II regions are useful probes of the past chemical composition of the interstellar medium. In particular, there are problems in modeling [O III] optical spectral features in planetary nebulae and HII regions to determine elemental abundance and electron temperature. There are discrepancies between the results derived from recombination lines and collisionally excited lines (Storey & Sochi 2015). The discrepancies have recently been investigated using κ -distributions for non-Maxwellian electron energy distributions (Nicholls et al. 2013; Mendoza & Bautista 2014; Storey & Sochi 2015) with no clear evidence of a departure from the Maxwell-Boltzmann electron energy distributions. The [O III] far-Infrared fine-structure lines have been observed in Seyfert galaxies with the Herschel-PACS spectrometer (Spinoglio et al. 2015). The [O III] line intensity ratios are density sensitive in the range of $10 \,\mathrm{cm}^{-3} < n_e < 10^4 \,\mathrm{cm}^{-3}$. Using the [O III] line ratio $\lambda 4363/(\lambda 4959 + \lambda 5007)$ and [S III] line ratio $\lambda 6312/(\lambda 9069 + \lambda 9352)$ Mendoza & Bautista (2014) and Binette et al. (2012) noted T(O III) < T(S III) in galactic and extragalactic H II regions.

The ultraviolet emissions from O III have been observed in Io plasma spectra by the Cassini Ultraviolet Imaging Spectrograph (UVIS) during the Cassini flyby of Jupiter (Steffl

et al. 2004a, 2004b; Delamere et al. 2005). The O III emission features due to the $2s^22p^2$ $^3P - 2s2p^3$ $^3P^o$ (833–835 Å), $2s2p^3$ $^3D^o - 2s^22p3p$ 3P (552–559 Å), $2s^22p^2$ $^3P - 2s2p^3$ $^3S^o$ (505-512 Å), and $2s^22p^2$ $^3P - 2s^22p3s$ $^3P^o$ (370-380 Å)transitions have been detected in the spectra of Io plasma torus by the Cassini and Extreme Ultraviolet Explorer. The intercombination lines due to the $2s^22p^2$ $^3P - 2s2p^3$ $^5S^o$ transitions in O III at 1666.15 Å and 1660.15 Å have been observed by the Hopkins Ultraviolet Telescope and Voyager. The spectral lines due to the $2s^22p^2$ $^3P_1 - 2s2p^3$ $^3D_{1,2}$ transitions have been observed by the Solar Ultraviolet Measurement of Emitted Radiation spectrometer (SUMER) in the lower solar transition region (Doschek et al. 2004). The fine-structure levels of a metastable term that decay by intercombination or forbidden type of transitions normally offer good density diagnostics. The ratios involving lines within the same multiplet $2s^22p^2$ $^3P - 2s2p^3$ $^3P^o$ of O III provide reliable density diagnostics. The intercombination lines due to the $2s^22p^2$ $^3P_{1,2}$ $-2s2p^3$ $^5S_2^o$ transitions in O III at 1666.15 Å and 1660.15 Å offer useful diagnostics of the Io-torus-Jupiter system and other astrophysical objects.

Several electron excitation collision and transition rate calculations for O²⁺ have previously been reported. Bhatia & Kastner (1993) presented collision strengths between fine-structure levels of O III, but they used limited configuration interaction (CI) in their distorted-wave calculations and did not include resonance effects. Aggarwal & Keenan (1999) used the 26-state *R*-matrix method (Berrington et al. 1995) and transformed LS reactance matrices into pair coupling. Lennon & Burke (1994) also performed a 12-state LS *R*-matrix plus pair coupling calculation for O²⁺. More recently, Breit–Pauli *R*-matrix (BPRM) calculations are

Index	Configuration	LSJ π	Exp ^a	Present	Diff. ^b	Diff. ^c	Diff.d	Diff. ^e	Lifetime (s)
1	$2s^22p^2$	$^{3}P_{0}$	0.000	0.000	0.000	0.000	0.000	0.000	
2	$2s^22p^2$	${}^{3}P_{1}$	0.014	0.014	0.000	0.000	0.000	0.000	3.97E + 04
3	$2s^22p^2$	${}^{3}P_{2}$	0.038	0.041	0.003	0.000	0.000	0.000	7.14E+03
4	$2s^22p^2$	$^{1}D_{2}$	2.514	2.518	0.004	0.148	0.012	0.016	3.89E + 01
5	$2s^22p^2$	${}^{1}S_{0}$	5.354	5.354	0.000	0.334	0.011	0.026	5.23E-01
6	$2s2p^3$	${}^{5}S_{2}^{o}$	7.479	7.470	-0.009	-0.092	0.026	-0.032	1.24E-03
7	$2s2p^{3}$	${}^{3}D_{3}^{o}$	14.881	14.893	0.012	0.217	0.054	0.009	1.62E-09
8	$2s2p^3$	${}^{3}D_{2}^{o}$	14.885	14.894	0.009	0.216	0.054	0.009	1.62E-09
9	$2s2p^3$	${}^{3}D_{1}^{o}$	14.885	14.894	0.009	0.217	0.055	0.009	1.61E-09
10	$2s2p^3$	${}^{3}P_{2}^{o}$	17.653	17.693	0.040	0.363	0.065	0.033	5.40E-10
11	$2s2p^3$	${}^{3}P_{1}^{o}$	17.653	17.693	0.040	0.363	0.065	0.033	5.38E-10
12	$2s2p^3$	${}^{3}P_{0}^{o}$	17.655	17.694	0.039	0.363	0.065	0.033	5.37E-10
13	$2s2p^{3}$	${}^{1}\!D_{2}^{o}$	23.192	23.222	0.030	0.490	0.076	0.039	1.83E-10
14	$2s2p^{3}$	${}^{3}S_{1}^{o}$	24.436	24.490	0.054	0.411	0.061	0.026	6.89E-11
15	$2s2p^3$	${}^{1}P_{1}^{o}$	26.094	26.167	0.073	0.636	0.090	0.088	9.02E-11
16	$2s^22p(^2P^o)3s$	${}^{3}P_{0}^{o}$	33.136	33.143	0.007	•••	0.072		2.52E-10
17	$2s^22p(^2P^o)3s$	${}^{3}P_{1}^{o}$	33.151	33.158	0.007	•••	0.072	•••	2.51E-10
18	$2s^22p(^2P^o)3s$	${}^{3}P_{2}^{o}$	33.182	33.189	0.007	•••	0.072	•••	2.51E-10
19	$2s^22p(^2P^o)3s$	${}^{1}\!P_{1}^{o}$	33.858	33.894	0.036	•••	0.079	•••	2.12E-10
20	$2p^{4}$	${}^{3}P_{2}$	35.182	35.214	0.032	0.604	0.116	•••	1.65E-10
21	$2p^{4}$	${}^{3}P_{1}$	35.209	35.239	0.030	0.605	0.116		1.64E-10
22	$2p^{4}$	$^{3}P_{0}$	35.220	35.251	0.031	0.605	0.116		1.64E-10
23	$2s^22p(^2P^o)3p$	${}^{1}P_{1}$	36.074	36.069	-0.005		0.088		5.23E-09
24	$2s^22p(^2P^o)3p$	$^{3}D_{1}$	36.435	36.435	0.000	•••	0.088		5.23E-09
25	$2s^22p(^2P^o)3p$	$^{3}D_{2}$	36.452	36.452	0.000	•••	0.088		5.22E-09
26	$2s^22p(^2P^o)3p$	$^{3}D_{3}$	36.479	36.478	-0.001	•••	0.088		2.27E-09
27	$2s^22p(^2P^o)3p$	${}^{3}S_{1}$	36.893	36.891	-0.002	•••	0.083		2.27E-09
28	$2p^{4}$	$^{1}D_{2}$	36.984	37.016	0.032	•••	0.083		4.26E-10
29	$2s^22p(^2P^o)3p$	${}^{3}P_{0}$	37.224	37.248	0.024	•••	0.136	•••	2.73E-09
30	$2s^22p(^2P^o)3p$	${}^{3}P_{1}$	37.234	37.258	0.024	•••	0.084	•••	2.72E-09
31	$2s^22p(^2P^o)3p$	${}^{3}P_{2}$	37.250	37.275	0.025	•••	0.084	•••	2.71E-09
32	$2s^22p(^2P^o)3p$	$^{1}D_{2}$	38.012	38.051	0.039	•••	0.084	•••	3.16E-09
33	$2s^22p(^2P^o)3p$	${}^{1}S_{0}$	38.907	38.959	0.052	•••	0.091	•••	1.56E-09
34	$2s^22p(^2P^o)3d$	${}^{3}F_{2}^{o}$	40.229	40.228	-0.001	•••	0.108	•••	2.13E-10
35	$2s^22p(^2P^o)3d$	${}^{3}F_{3}^{o}$	40.253	40.257	0.004	•••	0.080	•••	3.94E-09
36	$2s^22p(^2P^o)3d$	${}^{1}D_{2}^{o}$	40.262	40.258	-0.004	•••	0.081	•••	1.80E-10
37	$2s^22p(^2P^o)3d$	${}^{3}F_{4}^{o}$	40.275	40.279	0.004	•••	0.079	•••	5.03E-09
38	$2s^22p(^2P^o)3d$	${}^{3}D_{1}^{o}$	40.571	40.543	-0.028	•••	0.074	•••	4.93E-11
39	$2s^22p(^2P^o)3d$	${}^{3}D_{2}^{o}$	40.577	40.549	-0.028	•••	0.074	•••	4.94E-11
40	$2s^22p(^2P^o)3d$	${}^{3}D_{3}^{o}$	40.586	40.558	-0.028	•••	0.074	•••	4.94E-11
41	$2s^22p(^2P^o)3d$	${}^{3}P_{2}^{o}$	40.849	40.842	-0.007	•••	0.075	•••	8.50E-11
42	$2s^22p(^2P^o)3d$	${}^{3}P_{1}^{o}$	40.863	40.855	-0.008	•••	0.075	•••	8.50E-11
43	$2s^22p(^2P^o)3d$	${}^{3}P_{0}^{o}$	40.871	40.862	-0.009	•••	0.075	•••	8.50E-11
44	$2s^22p(^2P^o)3d$	${}^{1}F_{3}^{o}$	41.141	41.136	-0.005	•••	0.078	•••	5.19E-11
45	$2s^22p(^2P^o)3d$	${}^{1}P_{1}^{o}$	41.259	41.265	0.006	•••	0.079	•••	8.32E-11
46	$2s2p^{2}(^{4}P)3s$	⁵ P ₁	41.978	42.003	0.025	•••		•••	3.02E-10
47	$2s2p^{2}(^{4}P)3s$	⁵ P ₂	41.994	42.019	0.025	•••		•••	3.02E-10
48	$2s2p^{2}(^{4}P)3s$	${}^{5}P_{3}$	42.014	42.043	0.029	•••		•••	3.02E-10
49	$2p^4$	${}^{1}S_{0}$	42.565	42.629	0.064	•••	0.180	•••	1.67E-10
50	$2s2p^{2}(^{4}P)3s$	${}^{3}P_{0}$	43.398	43.473	0.075	•••	•••	•••	2.39E-10
51	$2s2p^2(^4P)3s$	${}^{3}P_{1}$	43.410	43.485	0.075	•••	•••	•••	2.39E-10
52	$2s2p^2(^4P)3s$	${}^{3}P_{2}$	43.431	43.510	0.079	•••	•••	•••	2.38E-10
53	$2s^22p(^2P^o)4s$	${}^{3}P_{0}^{o}$	44.230	44.163	-0.067	•••	•••	•••	5.44E-10
54	$2s^22p(^2P^o)4s$	${}^{3}P_{1}^{o}$	44.243	44.176	-0.067	•••	•••	•••	5.40E-10
55	$2s^22p(^2P^o)4s$	${}^{3}P_{2}^{o}$	44.277	44.209	-0.068	•••	•••	•••	5.41E-10
56	$2s^22p(^2P^o)4s$	${}^{1}P_{1}^{o}$	44.469	44.411	-0.058	•••	•••	•••	3.37E-10
57	$2s2p^{2}(^{4}P)3p$	${}^{3}S_{1}^{o}$	45.039	45.016	-0.023	•••	•••	•••	2.66E-10
58	$2s2p^{2}(^{4}P)3p$	${}^{5}D_{0}^{o}$	45.320	45.316	-0.004	•••	•••	•••	8.86E-09
59	$2s2p^{2}(^{4}P)3p$	${}^{5}D_{1}^{o}$	45.324	45.321	-0.003	•••	•••	•••	8.86E-09

Table 1 (Continued)

Index	Configuration	$LSJ\pi$	Exp ^a	Present	Diff.b	Diff.c	Diff.d	Diff. ^e	Lifetime (s)
60	$2s2p^{2}(^{4}P)3p$	$5D_2^o$	45.332	45.330	-0.002				8.86E-09
61	$2s^22p(^2P^o)4p$	${}^{1}P_{1}^{2}$	45.344	45.275	-0.069				1.73E-09
62	$2s2p^2(^4P)3p$	${}^{5}D_{3}^{o}$	45.345	45.343	-0.002				8.85E-09
63	$2s2p^{2}(^{4}P)3p$	$^{5}D_{4}^{o}$	45.361	45.362	0.001				8.83E-09
64	$2s^22p(^2P^o)4p$	$^{3}D_{1}$	45.439	45.373	-0.066				2.03E-09
65	$2s^22p(^2P^o)4p$	$^{3}D_{2}$	45.452	45.386	-0.066				2.03E-09
66	$2s^22p(^2P^o)4p$	$^{3}D_{3}^{2}$	45.478	45.411	-0.067				2.03E-09
67	$2s^22p(^2P^o)4p$	${}^{3}S_{1}$	45.620	45.556	-0.064				1.97E-09
68	$2s2p^{2}(^{4}P)3p$	${}^{5}P_{1}^{o}$	45.693	45.702	0.009	•••			6.66E-09
69	$2s2p^{2}(^{4}P)3p$	${}^{5}P_{2}^{o}$	45.700	45.711	0.011	•••			6.68E-09
70	$2s2p^{2}(^{4}P)3p$	${}^{5}P_{3}^{o}$	45.713	45.725	0.012	•••			6.65E-09
71	$2s^22p(^2P^o)4p$	${}^{3}P_{0}$	45.915	45.881	-0.034				2.62E-09
72	$2s^22p(^2P^o)4p$	${}^{3}P_{1}$	45.926	45.892	-0.034				2.61E-09
73	$2s^22p(^2P^o)4p$	${}^{3}P_{2}$	45.939	45.905	-0.034				2.66E-09
74	$2s^22p(^2P^o)4p$	$^{1}D_{2}$	45.986	45.941	-0.045				3.37E-09
75	$2s^22p(^2P^o)4p$	${}^{1}S_{0}$		46.314					3.20E-09
76	$2s2p^2(^4P)3p$	${}^{3}D_{1}^{o}$	46.441	46.475	0.034				1.11E-10
77	$2s2p^{2}(^{4}P)3p$	${}^{3}D_{2}^{o}$	46.452	46.487	0.035				1.11E-10
78	$2s2p^{2}(^{4}P)3p$	${}^{3}D_{3}^{0}$	46.469	46.505	0.036				1.09E-10
79	$2s2p^{2}(^{4}P)3p$	${}^{5}S_{2}^{o}$	46.628	46.672	0.044	•••	•••		2.93E-09
80	$2s^22p(^2P^o)4d$	${}^{3}F_{2}^{o}$	46.790	46.729	-0.061	•••	•••		7.09E-10
81	$2s^22p(^2P^o)4d$	${}^{3}F_{3}^{o}$	46.812	46.752	-0.060	•••	•••		2.68E-09
82	$2s^22p(^2P^o)4d$	${}^{1}D_{2}^{o}$	46.827	46.763	-0.064	•••			2.82E-10
83	$2s^{2}2p(^{2}P^{o})4d$	${}^{3}F_{4}^{o}$	46.835	46.775	-0.060				2.84E-09
84	$2s^{2}2p(^{2}P^{o})4d$	${}^{3}P_{2}^{o}$	46.916	46.889	-0.027				1.24E-10
85	$2s^{2}2p(^{2}P^{o})4d$	${}^{3}P_{1}^{o}$	46.918	46.895	-0.023				1.22E-10
86	$2s^{2}2p(^{2}P^{o})4d$	${}^{3}P_{0}^{o}$	46.920	46.899	-0.023				1.21E-10
87	$2s^{2}2p(^{2}P^{o})4d$	${}^{3}D_{1}^{o}$	47.018	46.976	-0.042				2.40E-10
88	$2s^{2}2p(^{2}P^{o})4d$	${}^{3}D_{2}^{o}$	47.026	46.985	-0.041				2.43E-10
89	$2s^{2}2p(^{2}P^{o})4d$	$^{3}D_{3}^{o}$	47.034	46.993	-0.041				2.54E-10
90	$2s^{2}2p(^{2}P^{o})4f$	${}^{1}F_{3}$	47.190	47.106	-0.084	•••			7.78E-10
91	$2s^{2}2p(^{2}P^{o})4f$	${}^{3}F_{2}$	47.191	47.108	-0.084	•••		•••	7.79E-10 7.79E-10
92	$2s^{2}2p(^{2}P^{o})4f$	${}^{3}F_{3}$	47.197	47.114	-0.083	•••		•••	7.79E-10 7.79E-10
93	$2s^{2}2p(^{2}P^{o})4f$	${}^{3}F_{4}$	47.199	47.114	-0.083			•••	7.75E=10 7.81E=10
94	$2s^{2}p(1) - y$ $2s^{2}2p(2P^{o})4d$	${}^{1}F_{3}^{o}$	47.202	47.110	0.035				1.05E-10
95	$2s^{2}2p(^{2}P^{o})4f$	${}^{1}_{3}G_{3}$	47.202	47.237	0.036	•••		•••	8.03E-10
96	$2s^{2}p(1)4f$ $2s^{2}2p(^{2}P^{o})4f$	${}^{3}G_{4}$	47.205	47.243	0.038				8.23E-10
90 97	$2s^{2}2p(^{1})^{4}$ $2s^{2}2p(^{2}P^{o})4d$	${}^{1}P_{1}^{o}$	47.203	47.243	-0.063				1.73E-10
98	$2s^{2}2p(^{2}P^{o})4f$	${}^{3}G_{5}$	47.211	47.148	-0.056				8.07E-10
99	$2s^{2}2p(^{2}P^{o})4f$ $2s^{2}2p(^{2}P^{o})4f$	$^{3}D_{3}$	47.249	47.178	-0.030 -0.082				8.22E-10
100	$2s^{2}p(P^{o})4f$ $2s^{2}2p(^{2}P^{o})4f$	$^{3}D_{2}$	47.264	47.178	-0.082 -0.082				8.48E-10
101	$2s^{2}p(P^{o})4f$ $2s^{2}2p(^{2}P^{o})4f$	$^{1}G_{4}$	47.288	47.182	-0.082 -0.082				8.79E-10
102	$2s^{2}p(1)4f$ $2s^{2}2p(^{2}P^{o})4f$	$^{3}D_{1}$	47.295	47.200	-0.082 -0.088				8.25E-10
102	$2s^{2}p(P^{o})4f$ $2s^{2}2p(^{2}P^{o})4f$	${}^{1}D_{2}$	47.293	47.207	-0.088 -0.087				8.59E-10
103	$2s^{2}p(P^{*})4j$ $2s^{2}p^{2}(^{4}P)3p$	${}^{3}P_{0}^{o}$	47.297	47.210	-0.087 -0.082		•••		3.42E-09
104	$2s2p^{2}(P)3p$ $2s2p^{2}(^{4}P)3p$	${}^{3}P_{1}^{o}$	47.297	47.213	-0.082 -0.088			•••	2.73E-09
105		${}^{3}P_{2}^{o}$				•••		•••	2.75E-09 2.86E-09
	$2s2p^{2}(^{4}P)3p$		47.318	47.230	-0.088	•••		•••	
107	$2s^22p(^2P^o)5s$	${}^{3}P_{0}^{o}$	48.581	48.500	-0.081	•••	•••	•••	7.26E-10
108	$2s^22p(^2P^o)5s$	${}^{3}P_{1}^{o}$	48.592	48.511	-0.081	•••	•••	•••	7.18E-10
109	$2s^22p(^2P^o)5s$	${}^{3}P_{2}^{o}$ ${}^{1}P_{2}^{o}$	48.628	48.546	-0.082	•••	•••	•••	7.20E-10
110	$2s^22p(^2P^o)5s$	${}^{1}P_{1}^{o}$	48.699	48.621	-0.078	•••	•••	•••	6.11E-10
111	$2s2p^{2}(^{4}P)3d$	${}^{5}F_{1}$	48.915	48.939	0.024	•••	•••	•••	5.55E-09
112	$2s2p^{2}(^{4}P)3d$	${}^{5}F_{2}$	48.920	48.945	0.025	•••	•••	•••	5.54E-09
113	$2s2p^{2}(^{4}P)3d$	⁵ F ₃	48.927	48.953	0.026	•••	•••	•••	5.53E-09
114	$2s2p^{2}(^{4}P)3d$	${}^{5}F_{4}$	48.937	48.964	0.027	•••	•••	•••	5.54E-09
115	$2s2p^{2}(^{4}P)3d$	⁵ F ₅	48.948	48.978	0.030	•••	•••	•••	5.56E-09
116	$2s2p^{2}(^{4}P)3d$	⁵ P ₃	49.364	49.400	0.036	•••	•••	•••	4.99E-11
117 118	$2s2p^2(^4P)3d$ $2s2p^2(^2D)3s$	${}^{5}P_{2}$	49.364	49.406	0.042	•••	•••	•••	5.36E-11
		$^{3}D_{1}$	49.363	49.411	0.048			•••	2.76E-10

Table 1 (Continued)

	(Continued)										
Index	Configuration	LSJ π	Exp ^a	Present	Diff. ^b	Diff.c	Diff.d	Diff.e	Lifetime (s)		
119	$2s2p^2(^4P)3d$	⁵ P ₁	49.364	49.414	0.050	•••			5.46E-11		
120	$2s2p^{2}(^{2}D)3s$	$^{3}D_{2}$	49.374	49.415	0.041	•••	•••	•••	2.90E-10		
121	$2s2p^{2}(^{2}D)3s$	$^{3}D_{3}$	49.406	49.362	-0.044	•••	•••	•••	2.96E-10		
122	$2s2p^2(^4P)3d$	$^{5}D_{0}$	49.415	49.372	-0.043				4.34E-09		
123	$2s2p^2(^4P)3d$	$^{5}D_{1}$	49.420	49.381	-0.039				2.54E-10		
124	$2s2p^2(^4P)3d$	$^{5}D_{2}$		49.378	•••		•••	•••	2.77E-10		
125	$2s2p^2(^4P)3d$	$^{5}D_{3}$		49.387	•••		•••	•••	4.48E-10		
126	$2s2p^2(^4P)3d$	$^{5}D_{4}$		49.397	•••		•••	•••	4.48E-09		
127	$2s2p^2(^4P)3d$	${}^{3}P_{2}$	49.637	49.651	0.014				1.18E-10		
128	$2s2p^2(^4P)3d$	${}^{3}P_{1}$	49.651	49.666	0.015				1.18E-10		
129	$2s2p^2(^4P)3d$	${}^{3}P_{0}$	49.658	49.673	0.015		•••	•••	1.18E-10		
130	$2s2p^2(^4P)3d$	$^{3}F_{2}$	49.764	49.777	0.013		•••	•••	1.10E-10		
131	$2s2p^2(^4P)3d$	${}^{3}F_{3}$	49.777	49.791	0.014		•••	•••	1.10E-10		
132	$2s2p^2(^4P)3d$	${}^{3}F_{4}$	49.793	49.809	0.016	•••	•••	•••	1.10E-10		
133	$2s2p^2(^2D)3s$	$^{1}D_{2}$		50.231	•••	•••	•••	•••	4.17E-10		
134	$2s2p^2(^4P)3d$	$^{3}D_{1}$	50.313	50.342	0.029	•••	•••	•••	1.16E-10		
135	$2s2p^2(^4P)3d$	$^{3}D_{2}$	50.317	50.347	0.030	•••	•••	•••	1.16E-10		
136	$2s2p^2(^4P)3d$	$^{3}D_{3}$	50.323	50.354	0.031	•••	•••	•••	1.15E-10		
137	$2s2p^2(^2D)3p$	${}^{3}F_{2}^{o}$	•••	52.528	•••	•••	•••	•••	1.85E-09		
138	$2s2p^2(^2D)3p$	${}^{3}F_{3}^{o}$	•••	52.530	•••	•••	•••	•••	1.87E-09		
139	$2s2p^2(^2D)3p$	${}^{3}F_{4}^{o}$		52.532	•••	•••	•••	•••	1.89E-09		
140	$2s2p^2(^2D)3p$	${}^{3}D_{1}^{o}$	•••	52.705	•••	•••	•••	•••	1.04E-09		
141	$2s2p^2(^2D)3p$	${}^{3}D_{2}^{o}$	•••	52.706	•••	•••	•••	•••	1.04E-09		
142	$2s2p^2(^2D)3p$	${}^{3}D_{3}^{o}$	•••	52.709	•••	•••	•••	•••	1.05E-09		
143	$2s2p^2(^2D)3p$	${}^{1}D_{2}^{o}$		52.983	•••	•••	•••	•••	2.62E-10		
144	$2s2p^2(^2D)3p$	${}^{1}F_{3}^{o}$	52.859	52.788	-0.071				2.57E-10		
145	$2s2p^2(^2D)3p$	${}^{3}P_{0}^{o}$	•••	53.206	•••		•••	•••	6.84E-10		
146	$2s2p^2(^2D)3p$	${}^{3}P_{1}^{o}$	•••	53.208	•••		•••	•••	6.91E-10		
147	$2s2p^2(^2D)3p$	${}^{3}P_{2}^{o}$		53.213	•••	•••	•••	•••	7.05E-10		
148	$2s2p^2(^2D)3p$	${}^{1}P_{1}^{o}$	53.317	53.391	0.074	•••	•••	•••	1.81E-10		
149	$2s2p^2(^2S)3s$	${}^{3}S_{1}$	•••	53.717	•••	•••	•••	•••	1.12E-10		
150	$2s2p^2(^2S)3s$	${}^{1}S_{0}$	•••	54.542	•••	•••	•••	•••	2.58E-10		
151	$2s2p^2(^2D)3d$	${}^{3}F_{2}$	•••	55.535	•••	•••	•••	•••	5.89E-10		
152	$2s2p^2(^2D)3d$	${}^{3}F_{3}$	•••	55.542	•••	•••	•••	•••	5.62E-10		
153	$2s2p^2(^2D)3d$	${}^{3}F_{4}$	•••	55.550	•••	•••	•••	•••	5.27E-10		
154	$2s2p^2(^2P)3s$	${}^{3}P_{0}$	•••	55.798	•••	•••	•••	•••	8.29E-11		
155	$2s2p^{2}(^{2}P)3s$	${}^{3}P_{1}$	•••	55.806	•••	•••	•••	•••	7.95E-11		
156	$2s2p^{2}(^{2}P)3s$	${}^{3}P_{2}$	•••	55.827	•••	•••	•••	•••	7.85E-11		
157	$2s2p^2(^2D)3d$	${}^{3}G_{3}$	•••	56.209	•••	•••	•••	•••	9.12E-10		
158	$2s2p^2(^2D)3d$	${}^{3}G_{4}$	•••	56.212	•••	•••	•••	•••	9.02E-10		
159	$2s2p^2(^2D)3d$	${}^{3}G_{5}$	•••	56.214	•••	•••	•••	•••	9.21E-10		
160	$2s2p^2(^2D)3d$	${}^{1}F_{3}$	•••	56.273	•••	•••	•••	•••	1.56E-10		
161	$2s2p^2(^2D)3d$	$^{3}D_{1}$	56.311	56.317	0.006	•••	•••	•••	6.03E-11		
162	$2s2p^{2}(^{2}D)3d$	$^{3}D_{2}$	56.311	56.318	0.007	•••		•••	6.05E-11		
163	$2s2p^2(^2D)3d$	$^{3}D_{3}$	56.311	56.320	0.009	•••	•••	•••	6.09E-11		
164	$2s2p^{2}(^{2}P)3s$	${}^{1}P_{1}$	•••	56.360	•••	•••	•••	•••	6.57E-11		
165	$2s2p^{2}(^{2}D)3d$	${}^{1}G_{4}$		56.531		•••	•••	•••	1.27E-09		
166	$2s2p^{2}(^{2}D)3d$	${}^{3}P_{0}$	56.732	56.775	0.043	•••		•••	9.49E-11		
167	$2s2p^{2}(^{2}D)3d$	${}^{3}P_{1}$	56.732	56.776	0.044	•••	•••	•••	9.51E-11		
168	$2s2p^{2}(^{2}D)3d$	${}^{3}P_{2}$	56.732	56.777	0.045	•••		•••	9.56E-11		
169	$2s2p^{2}(^{2}D)3d$	$^{1}D_{2}$		56.944		•••		•••	8.06E-11		
170	$2s2p^{2}(^{2}D)3d$	${}^{1}P_{1}$	•••	57.039		•••	•••	•••	1.25E-10		
171	$2s2p^{2}(^{2}D)3d$	${}^{3}S_{1}$	•••	57.158	•••	•••	•••	•••	1.26E-10		
172	$2s2p^2(^2S)3p$	${}^{3}P_{0}^{o}$	•••	57.594	•••	•••	•••	•••	4.86E-10		
173	$2s2p^{2}(^{2}S)3p$	${}^{3}P_{1}^{o}$	•••	57.602	•••	•••	•••	•••	4.47E-10		
174	$2s2p^{2}(^{2}S)3p$	${}^{3}P_{2}^{o}$	•••	57.617	•••	•••	•••	•••	4.89E-10		
175	$2s2p^2(^2S)3p$	${}^{1}P_{1}^{o}$	•••	57.647	•••	•••	•••	•••	1.30E-10		
176	$2s2p^2(^2D)3d$	${}^{1}S_{0}$	•••	57.739	•••	•••	•••	•••	1.44E-10		
177	$2s2p^2(^2P)3p$	${}^{1}S_{0}^{o}$	•••	58.280	•••	•••	•••	•••	1.21E-10		

Table 1 (Continued)

Index	Configuration	$\mathrm{LSJ}\pi$	Exp ^a	Present	Diff.b	Diff. ^c	Diff.d	Diff.e	Lifetime (s)
178	$2s2p^{2}(^{2}P)3p$	${}^{3}D_{1}^{o}$		58.937	•••	•••		•••	1.71E-10
179	$2s2p^{2}(^{2}P)3p$	${}^{3}D_{2}^{o}$		58.947					1.68E-10
180	$2s2p^{2}(^{2}P)3p$	${}^{3}D_{3}^{o}$		58.965					1.67E-10
181	$2s2p^{2}(^{2}P)3p$	${}^{3}P_{0}^{o}$		59.312					1.42E-10
182	$2s2p^2(^2P)3p$	${}^{3}P_{1}^{o}$		59.317					1.42E-10
183	$2s2p^2(^2P)3p$	${}^{3}P_{2}^{o}$		59.327					1.42E-10
184	$2s2p^{2}(^{2}P)3p$	${}^{3}S_{1}^{o}$		59.774					1.05E-10
185	$2s2p^{2}(^{2}P)3p$	${}^{1}\!D_{2}^{o}$		59.816					1.68E-10
186	$2s2p^{2}(^{2}P)3p$	${}^{1}P_{1}^{o}$		60.464					1.46E-10
187	$2s2p^{2}(^{2}S)3d$	$^{3}D_{2}$		60.797					1.42E-10
188	$2s2p^2(^2S)3d$	$^{3}D_{3}$	•••	60.797		•••			1.41E-10
189	$2s2p^2(^2S)3d$	$^{3}D_{1}$	•••	60.797		•••			1.41E-10
190	$2s2p^{2}(^{2}S)3d$	$^{1}D_{2}$	•••	61.203	•••	•••		•••	1.70E-10
191	$2s2p^{2}(^{2}P)3d$	${}^{1}P_{1}$	•••	62.901	•••	•••		•••	1.44E-10
192	$2s2p^{2}(^{2}P)3d$	$^{3}F_{2}$		62.908					1.06E-10
193	$2s2p^{2}(^{2}P)3d$	${}^{3}F_{3}$	•••	62.919	•••	•••		•••	1.06E-10
194	$2s2p^{2}(^{2}P)3d$	$^{3}F_{4}$	•••	62.951	•••	•••		•••	1.06E-10
195	$2s2p^{2}(^{2}P)3d$	${}^{3}P_{0}$	•••	62.954	•••	•••		•••	7.56E-11
196	$2s2p^{2}(^{2}P)3d$	${}^{3}P_{1}$	•••	62.958	•••	•••		•••	7.23E-11
197	$2s2p^{2}(^{2}P)3d$	${}^{3}P_{2}$	•••	63.068	•••	•••		•••	6.82E-11
198	$2s2p^{2}(^{2}P)3d$	$^{3}D_{1}$	•••	63.195	•••	•••		•••	1.16E-10
199	$2s2p^{2}(^{2}P)3d$	$^{3}D_{3}$	•••	63.196	•••	•••		•••	1.19E-10
200	$2s2p^{2}(^{2}P)3d$	$^{3}D_{2}$	•••	63.198	•••	•••	•••	•••	1.17E-10
201	$2s2p^{2}(^{2}P)3d$	${}^{1}F_{3}$	•••	63.384	•••	•••	•••	•••	4.67E-11
202	$2s2p^{2}(^{2}P)3d$	$^{1}D_{2}$		63.736					5.31E-11

Notes

reported by Palay et al. (2012) and Storey et al. (2014) who considered 19 and 146 fine-structure levels, respectively, and reported thermally averaged collision strengths for forbidden transitions among the lowest five levels giving rise to optical and infrared lines. There are significant discrepancies between these two latest calculations, up to 100% for some optical lines at lower temperatures. Nahar (1998) calculated radiative data in a close-coupling approximation by including one-body Breit-Pauli operators. Jönsson & Bieroń (2010) calculated energy levels and transition probabilities for the $2s^22p^2$ – $2s2p^3$ transitions in a carbon-like sequence including O²⁺. They used the multiconfiguration Dirac-Hartree-Fock (MCDHF) method (Jönsson et al. 2007) and included core-core, core-valence, and valence-electron correlation effects. Tachiev & Froese Fischer (2001) and Froese Fischer & Tachiev (2004) presented energy levels, lifetimes, and transition probabilities for the carbon-like and other sequences using the multiconfiguration Hartree-Fock (MCHF) method (Froese Fischer 2007) in the Breit-Pauli approach. Froese Fischer et al. (2009) presented an analysis of the accuracy of calculated transition probabilities for O²⁺ using the Breit–Pauli approach and included one-body and two-body Breit-Pauli operators. They also calculated transition probabilities for the forbidden transitions with the MCDHF method. The experimental lifetimes are available for some levels measured using various techniques. Träbert et al. (2000) used a heavy-ion storage ring and Smith et al. (2004) used an electron

cyclotron ion source to measure the lifetime of the $2s^22p^2$ 1S_0 level. The direct measurement of the time dependence of the spontaneous emission of O^{2+} ions was used to determine the experimental lifetime of the metastable $^5S_2^o$ level. Pinnington et al. (1974, 1978) and Baudinet-Robinet et al. (1991) made beam-foil measurements of lifetimes.

Our effort in the present work is to resolve discrepancies between the recent BPRM calculations of thermally averaged collision strengths for optical lines and, more importantly, to present electron excitation rates and transition rates for infrared to extreme ultraviolet (EUV) lines suitable for diagnostic calculations of gaseous nebulae, Io plasma torus, and the solar atmosphere. We present a more elaborate and accurate calculation for the electron scattering from O²⁺ by using highly accurate target wave functions and by including finestructure effects in the close-coupling expansions directly. The present calculations have been carried out with the B-spline Breit–Pauli R-matrix (BSR) code (Zatsarinny 2006). This code uses flexible term-dependent orbital sets to represent the target states as well as the scattering system. The term-dependent orbitals are determined by optimization on different target states independently. The use of term-dependent orbitals allows a more accurate target description than the previous collision calculations. We present collisional and radiative parameters for all transitions between 202 LSJ levels of O²⁺ covering the energy region from the ground $2s^22p^2$ configuration up to the

^a Experimental Energy Levels from NIST.

^b Difference between the present calculation and the experiment.

^c Difference between the AUTOSTRUCTURE calculation of Storey et al. (2014) and the experiment.

^d Difference between the MCHF calculation of Froese Fischer et al. (2009) and the experiment.

^e Difference between the MCDHF calculation of Jönsson & Bieroń (2010) and the experiment.

excited $2s^22p5s$ configuration. It includes all strong transitions from the 3s to 3p and 3d levels. In addition, the collisional and radiative parameters from our calculations can provide an independent check on the existing data sets for O^{2+} .

2. Computational Methods

2.1. Structure Calculations

In the present calculations, the 202 target levels of O²⁺ have been generated by combining the MCHF and the B-spline box-based multichannel methods (Zatsarinny & Froese Fischer 2009) and the structure of multichannel target expansions has been chosen as

$$\begin{split} \Phi^{J} &= \sum_{nl, \text{LS}} \{\phi(2s^{2}2p)P(nl)\}^{\text{LSJ}} + \sum_{nl, \text{LS}} \{\phi(2s2p^{2})P(nl)\}^{\text{LSJ}} \\ &+ \sum_{nl, \text{LS}} \{\phi(2p^{3})P(nl)\}^{\text{LSJ}} + \sum_{nl, \text{LS}} \{\phi(2s^{2}3s)P(nl)\}^{\text{LSJ}} \\ &+ \sum_{nl, \text{LS}} \{\phi(2s^{2}3d)P(nl)\}^{\text{LSJ}} + a_{\text{LSJ}}\varphi(2s^{2}2p^{2})^{\text{LSJ}} \\ &+ b_{\text{LSJ}}\varphi(2s2p^{3})^{\text{LSJ}}, \end{split}$$
(1)

where P(nl) represents the wave function of the valence electrons and the first two terms in the above expansion represent the entire $2s^22pnl$ and $2s2p^2nl$ Rydberg series in O^{2+} . The lower states belonging to the $2s^22p^2$ and $2s2p^3$ configurations have been represented with individual CI expansions φ . The short-range correlation effect has been included through the CI expansions of the $\phi(2s^22p)$ and $\phi(2s2p^2)$ ionic states. Additional long-range correlation effects have been included through the use of other terms in the above multichannel target expansion with ionic states $2p^3$, $2s^23s$, and $2s^23d$. The MCHF code (Froese Fischer 2007) has been used to generate the ϕ and φ expansions in separate multiconfiguration calculations. We included all single and double excitations from the 2s and 2p orbitals to the 3l and 4l (l = 0-3) correlated orbitals to generate these expansions separately for each configuration. In order to keep the final expansions for the O²⁺ states to a reasonable size, the configurations with expansion coefficients of magnitude less than 0.01 were omitted in our calculations. A separate CI expansion has been generated for the ground $2s^22p^2$ state, which included relaxation effects via state-specific one-electron orbitals.

The valence–electron functions P(nl) have been expanded in a B-spline basis and have been subjected to the condition that the wave functions vanish at the boundary. The B-spline coefficients for the valence-electron functions P(nl) and the coefficients $(a,b)_{LSJ}$ for the $2s^22p^2$ and $2s2p^3$ states have been obtained by diagonalizing the atomic Breit-Pauli Hamiltonian. All one-electron relativistic corrections have been included in the Breit-Pauli Hamiltonian. Thus we have generated a set of term-dependent one-electron orbitals for valence electrons and have also accounted for important interactions between the Rydberg series and the perturbers $2s2p^3$. Our calculations yield different nonorthogonal sets of orbitals for each atomic state. The configuration expansions for the atomic target states contained from 400 to 800 configurations for each state and hence could be used in the collision calculations with available computational resources.

2.2. Scattering Calculations

The BSR code (Zatsarinny 2006) has been employed in our scattering calculations. The details of the BSR method can be found in our previous calculations (Tayal & Zatsarinny 2011, 2014). The specific features of the present scattering calculation for O²⁺ are given here. We included 202 target states in the close-coupling expansions and this involved up to 922 different scattering channels in the JK-coupling scheme. The internal region radius was chosen to be 20 a_0 (a_0 is the Bohr radius) and the continuum orbitals were represented with 77 B-splines of the order of 8. It results in the Hamiltonian matrices with dimensions of up to 70,000, which needs to be diagonalized. It required the parallelized version of the BSR code, and we used up to 256 processors for a given partial wave. The Hamiltonian matrices directly include all one-electron relativistic corrections. Our numerical calculations included 52 partial waves with total momentum up to 2J = 51. The present calculations used huge configuration expansions for the total scattering functions, which include up to 1,700,000 individual configuration states. The calculation of required angular coefficients and the subsequent set-up of the Hamiltonian matrix needed further optimization of the code.

The parallel version of the STGF program (Badnell 1999) has been used to determine the asymptotic solutions in the outer region and subsequently the collision parameters. The narrow resonance structures in the energy range up to the highest excitation threshold at 4.5 Ry have been resolved by using the fine energy mesh of $10^{-5}z^2$ Ry. The collision strengths do not contain resonances at higher energies, where all channels are open. We used a coarse energy grid of 0.2 Ry up to 30 Ry in this energy region. The built-in top-up procedures in the STGF code have been employed to obtain converged collision strengths at higher energies.

The effective collision strength is a function of electron temperature and is determined by thermally averaging collision strengths over a Maxwellian distribution for a wide temperature range from $\log T = 2$ to $\log T = 5$ suitable for astrophysical and other plasma applications. For thermal averaging over Maxwellian electron energy distribution, the collision strengths at higher electron energies are needed. We extrapolated our numerical collision strengths using well-established asymptotic behavior of collision strengths at higher energies depending on the type of transition (Tayal & Zatsarinny 2011). Note that due to strong term-mixing, the appropriate asymptotic behavior for the particular transition was determined based on the numerical behavior of collision strengths at energies around E = 30 Ry.

3. Results and Discussion

3.1. Target Energies and Radiative Parameters

Our calculated target level excitation energies for the $202~{\rm O}^{2+}$ LSJ π levels included in the present scattering calculations have been compared with the available experimental values from the NIST compilation (Kramida et al. 2013) in Table 1. The parity π is shown only for odd parity levels. We compare differences between the present calculated and experimental values with other available calculations of Storey et al. (2014), Froese Fischer et al. (2009), and Jönsson & Bieroń (2010). Storey et al. (2014), Froese Fischer et al. (2009), and the present work used a semi-relativistic Breit–Pauli approach using the AUTOSTRUCTURE, MCHF, and MCHF plus BSR computer codes (Badnell 2011; Froese Fischer 2007; Zatsarinny & Froese

Table 2Transition Rates in s⁻¹

Transition	$A_L(P)$	$A_V(P)$	$A_L(MCDHF)$	A_V (MCDHF)	A_L (MCHF)	$A_L(CIV3)$	A(NIST)
$2s^22p^2 {}^3P_0 - 2s2p^3 {}^3D_1^o$	3.50+08	3.62+08	3.50+08	3.51+08	3.489+08	3.505+08	3.41+08
$2s^22p^2 {}^{3}P_0 - 2s2p^3 {}^{3}P_1^o$	6.17 + 08	6.65 + 08	6.11 + 08	6.07 + 08	6.112 + 08	6.595 + 08	6.06+09
$2s^22p^2 {}^3P_0 - 2s2p^3 {}^3S_1^o$	1.61+09	1.74+09	1.59+09	1.58+09	1.588+09	1.718+09	1.61+09
$2s^22p^2 {}^3P_0 - 2s2p^3 {}^1P_1^o$	6.69 + 04	7.52 + 04	5.09+04	5.25 + 04	6.279 + 04	2.400+04	
$2s^22p^2 {}^3P_1 - 2s2p^3 {}^5S_2^o$	2.20+02	4.50+02	2.15+02	3.79+02	3.79+02	2.308+02	1.61 + 02
$2s^22p^2 {}^3P_1 - 2s2p^3 {}^3D_2^o$	4.71 + 08	4.88 + 08	4.71 + 08	4.73 + 08	4.693 + 08	4.716 + 08	4.58 + 08
$2s^22p^2 {}^3P_1 - 2s2p^3 {}^3D_1^o$	2.55 + 08	2.64 + 08	2.55 + 08	2.56+08	2.542 + 08	2.564 + 08	2.48 + 08
$2s^22p^2 {}^{3}P_{1} - 2s2p^3 {}^{3}P_{2}^{o}$	4.55 + 08	4.91 + 08	4.50 + 08	4.47 + 08	4.506 + 08	4.871 + 08	4.47 + 08
$2s^22p^2 {}^3P_1 - 2s2p^3 {}^3P_1^o$	4.75 + 08	5.12+08	4.70 + 08	4.67 + 08	4.706 + 08	5.060+08	4.66 + 08
$2s^22p^2 {}^3P_1 - 2s2p^3 {}^3P_0^o$	1.86+09	2.01+09	1.84 + 09	1.83 + 09	1.845 + 09	1.987 + 09	1.83+09
$2s^22p^2 {}^3P_1 - 2s2p^3 {}^1D_2^o$	1.53 + 04	1.49+04	1.26+04	1.10+04	1.325 + 04	1.175 + 04	
$2s^22p^2 {}^3P_1 - 2s2p^3 {}^3S_1^o$	4.84 + 09	5.22+09	4.77 + 09	4.74 + 09	4.765 + 09	5.175 + 09	4.82 + 09
$2s^22p^2 {}^3P_1 - 2s2p^3 {}^1P_1^o$	9.04 + 05	9.65 + 05	8.40 + 05	8.29 + 05	8.959 + 05	4.937 + 05	
$2s^22p^2 {}^3P_2 - 2s2p^3 {}^5S_2^o$	6.02 + 02	1.05+03	5.35 + 02	1.03 + 03	5.765 + 02	4.148 + 02	
$2s^22p^2 {}^3P_2 - 2s2p^3 {}^3D_3^o$	6.15 + 08	6.38 + 08	6.17 + 08	6.19 + 08	6.138 + 08	6.182 + 08	5.99 + 08
$2s^22p^2 {}^3P_2 - 2s2p^3 {}^3D_2^o$	1.48 + 08	1.53 + 08	1.49 + 08	1.49 + 08	1.478 + 08	1.497 + 08	1.44 + 08
$2s^22p^2 {}^3P_2 - 2s2p^3 {}^3D_1^o$	1.60+07	1.66+07	1.61 + 07	1.61 + 07	1.603+07	1.629 + 07	
$2s^22p^2 {}^3P_2 - 2s2p^3 {}^3P_2^o$	1.40+09	1.51+09	1.39+09	1.38+09	1.387 + 09	1.493 + 09	1.37+09
$2s^22p^2 {}^3P_2 - 2s2p^3 {}^3P_1^o$	7.67 + 08	8.26 + 08	7.60+08	7.54 + 08	7.608 + 08	8.192 + 08	7.54 + 08
$2s^22p^2 {}^3P_2 - 2s2p^3 {}^1D_2^o$	2.57 + 05	2.68+05	2.78 + 05	2.65 + 05	2.811 + 05	1.885 + 05	
$2s^22p^2 {}^{3}P_2 - 2s2p^3 {}^{3}S_1^o$	8.06 + 09	8.71 + 09	7.96 + 09	7.92+09	7.948+09	8.603 + 09	8.04 + 09
$2s^22p^2 {}^3P_2 - 2s2p^3 {}^1P_1^o$	2.16+05	2.25 + 05	1.81 + 05	1.78 + 05	1.947 + 05	3.894 + 04	
$2s^22p^2 {}^1D_2 - 2s2p^3 {}^5S_2^o$	7.74-03	8.84-03	6.07-03	5.94-02	5.777-03	9.213-04	
$2s^22p^2 {}^1D_2 - 2s2p^3 {}^3D_3^o$	1.89 + 04	2.13+04	2.01 + 04	2.33+04	2.108+04	1.329 + 04	
$2s^22p^2 {}^1D_2 - 2s2p^3 {}^3D_2^o$	4.33 + 03	5.02+03	4.04 + 03	4.80 + 03	4.003 + 03	2.425 + 03	
$2s^22p^2 {}^1D_2 - 2s2p^3 {}^3D_1^o$	2.43+03	4.06+03	2.13+03	3.42+03	2.358+03	2.239+03	
$2s^22p^2 {}^1D_2 - 2s2p^3 {}^3P_2^o$	5.48 + 03	4.98 + 03	6.71 + 03	5.62 + 03	7.088+03	2.524+03	
$2s^22p^2 {}^1D_2 - 2s2p^3 {}^3P_1^o$	2.57 + 04	2.89+04	2.72 + 04	2.89 + 04	2.746+04	2.024+04	
$2s^22p^2 {}^1D_2 - 2s2p^3 {}^1D_2^o$	5.46+09	5.91 + 09	5.48 + 09	5.45 + 09	5.463 + 09	5.561 + 09	5.41 + 09
$2s^22p^2 {}^1D_2 - 2s2p^3 {}^3S_1^o$	3.33+05	3.65 + 05	2.37 + 05	2.29+05	3.093+05	1.030+05	
$2s^22p^2 {}^1D_2 - 2s2p^3 {}^1P_1^o$	9.60+09	1.04 + 10	9.23 + 09	9.09+09	9.380+09	1.071 + 10	9.60+09
$2s^22p^2 {}^1S_0 - 2s2p^3 {}^3D_1^o$	1.70+03	1.62+03	1.86 + 03	1.65 + 03	1.699+03	8.307 + 02	
$2s^22p^2 {}^{1}S_0 - 2s2p^3 {}^{3}P_1^o$	9.52 + 03	1.23+04	1.03 + 04	1.15+04	9.578 + 03	6.108 + 03	
$2s^22p^2 {}^1S_0 - 2s2p^3 {}^3S_1^o$	6.73 + 04	7.16+04	6.56 + 04	6.73 + 04	6.975 + 04	2.168+03	
$2s^22p^2 {}^1S_0 - 2s2p^3 {}^1P_1^o$	1.49+09	1.60+09	1.60+09	1.62+09	1.508+09	1.500+09	1.49+09

Configuration	Level	Present	Other Theory	Experiment
$2s^22p^2$	^{1}S	523	523(a)	530 ± 25(b)
			559(k)	$540 \pm 27(c)$
$2s2p^{3}$	$^{5}S^{o}$	1.24	1.24(a); 1.33(d);	1.22 ± 0.08 (e)
			1.32(f); 1.21(f);	1.25(b)
			1.72(g)	
	$^3D^o$	1.62	1.62(a); 1.57(l); 1.63(m)	$1.61 \pm 0.06(h)$
	$^{3}P^{o}$	0.540	0.544(a); 0.434(l); 0.530(m)	$0.575 \pm 0.018(h)$
	$^1\!D^o$	0.183	0.183(a); 0.175(l); 0.183(m)	$0.20 \pm 0.05(h)$
	$^3S^o$	0.069	0.070(a); 0.064(l); 0.069(m)	$0.079 \pm 0.04(h)$
	$^{1}P^{o}$	0.090	0.092(a); 0.080(l); 0.090(m)	$0.087 \pm 0.011(h)$
$2s^22p(^2P^o)3s$	$^{3}P^{o}$	0.251	0.255(a); 0.262(l); 0.253(m)	$0.266 \pm 0.011(i)$
-	$^1\!P^o$	0.212	0.214(a); 0.228(l); 0.215(m)	$0.227 \pm 0.011(i)$ $0.17 \pm 0.01(j)$

References. (a) Froese Fischer et al. (2009); (b) Träbert et al. (2000); (c) Smith et al. (2004); (d) Jönsson & Bieroń (2010); (e) Johnson et al. (1984); (f) Fleming & Brage (1997). Using CIV3 and MCDF codes: (g) Aggarwal et al. (1997); (h) Pinnington et al. (1974); (i) Pinnington et al. (1978); (j) Baudinet-Robinet et al. (1991); (k) Galavs et al. (1997); (l) Nahar (1998); (m) Luo et al. (1989).

Table 4 Line Strengths (S), Oscillator Strengths (f_{ik}), and Transition Probabilities ($A_{k\ell}(s^{-1})$) for E1, M1, E2, and M2 Transitions

Туре	i	k	$\lambda(ext{Å})$	S	f_{ik}	A_{ki}
M1	1	2	895324.81	2.01E+00	9.07E-09	2.52E-05
E2	1	3	303482.66	5.06E-01	3.04E-15	4.41E-11
E2	1	4	4923.43	3.22E-05	4.53E-14	2.49E-06
M2	1	6	1659.78	7.78E-06	3.80E-18	1.84E-09
M2	1	8	832.46	8.08E+00	3.13E-11	6.03E-02
E1	1	9	832.46	2.99E-01	1.09E-01	3.50E+08
M2	1	10	700.73	1.10E+00	7.17E-12	1.95E-02
E1	1	11	700.73	3.14E-01	1.36E-01	6.17E+08
M2	1	13	533.90	4.51E-05	6.63E-16	3.10E-06
E1	1	14	506.26	3.10E-01	1.86E-01	1.61E+09
E1	1	15	473.82	1.05E-05	6.76E-06	6.69E+04
E1	1	17	373.91	1.03E-01	8.33E-02	1.32E+09

(This table is available in its entirety in machine-readable form.)

Lower Level	Upper Level	$\lambda(\mathring{\mathrm{A}})$	Present	CFF(a)	CFF(b)	SZ(c)
$2s^22p^2 {}^3P_2$	$2s^22p^2 \ ^1D_2$	5008	1.910–2	2.025-2	1.968-2	2.046–2
$2s^22p^2 {}^3P_1$	$2s^22p^2 {}^1D_2$	4960	6.574-3	6.946-3	6.526-3	6.791-3
$2s^22p^2 {}^3P_0$	$2s^22p^2 {}^1D_2$	4933	2.490-6	2.471-6	2.664-3	

References. (a) Froese Fischer et al.: BP II (2009); (b) Froese Fischer et al.: MCDHF II (2009); (c) Storey & Zeippen (2000).

Table 6 Line Intensity Ratios for the $2s^22p^2$ $^3P_{0,1,2}$ $^{-1}D_2$ Transitions

Intensity Ratio	Present	CFF(BP II)(a)	CFF(MCDHF)(b)	SZ(c)	Observation
I(5006.86)/I(4958.93)	2.905	3.016	2.993	3.013	2.966(d); 3.00(e); 2.909(f); 2.909(g)
I(4933.00)/I(4958.93)	3.790-4	3.558-4	4.082-4		3.82-4(d); 4.06-4(f); 4.20-4(g)

References. (a) Froese Fischer et al. (2009); (b) Froese Fischer et al. (2009); (c) Storey & Zeippen (2000); (d) Baldwin et al. (2000); (e) Rubin et al. (2003); (f) Esteban et al. (2004); (g) García-Rojas et al. (2006).

Fischer 2009), respectively, while Jönsson & Bieroń (2010) reported results from the fully relativistic MCDHF approach (Jönsson et al. 2007) with vacuum polarization and self-energy correction QED effects. Our calculated target energies differ from the experimental values on an average by about 0.035 eV. varying from 0.000 eV to 0.088 eV. The present energies show differences of ≥ 0.05 for the levels of $2s2p^2(^4P)3s$, $2s^22p4f$, $2s2p^2(^4P)3p$, and $2s^22p5s$ configurations because of the exclusion of configurations with small mixing coefficients from CI expansions. There is strong mixing between the levels of the $2s2p^23p$ and $2s^22p4d$ configurations. Based on the dominant weight in our calculation, the assignment of the configuration levels 84–86 is $2s^22p4d$ and 104–106 levels is $2s2p^23p$ respectively. However, these assignments differ from the NIST assignments. Though Storey et al. (2014) considered 146 target levels in their scattering calculations, they reported target energies for the 18 levels of the $2s^22p^2$, $2s2p^3$, and $2p^4$ configurations in their paper. The calculation of Storey et al. (2014) differs from the experiment on average by 0.315 eV and shows the largest difference of 0.636 eV for the $2s2p^3 \, ^1P_1^o$ level, while our calculation differs by 0.073 eV. The present MCHF plus multichannel B-spline box-based results are in better agreement with the MCHF calculation of Froese Fischer et al. (2009) and the experiment than the calculation of Storey et al. (2014). The MCHF calculation of Froese Fischer et al. (2009) shows the largest difference for the $2p^4$ 1S_0 level of 0.18 eV compared to 0.064 eV from the present work. Our excitation energies agree very well with the fully relativistic calculation of Jönsson & Bieroń (2010) and represent significant improvement over the AUTOSTRUCTURE calculation of Storey et al. (2014).

The comparison of transition rates for the $2s^22p^2 - 2s2p^3$ transitions between the present Breit–Pauli BSR results and the fully relativistic calculation of Jönsson & Bieroń (2010), the Breit–Pauli MCHF calculation of Froese Fischer et al. (2009), and the CIV3 (Hibbert 1975) calculation of Aggarwal et al. (1997) is given in Table 2. The available data from the NIST compilation are also shown. The present and MCDHF transition rates are shown in both length and velocity formulations. There is a good agreement between the present length and velocity results indicated by $A_L(P)$ and $A_L(V)$, respectively, especially for the dipole-allowed transitions. The

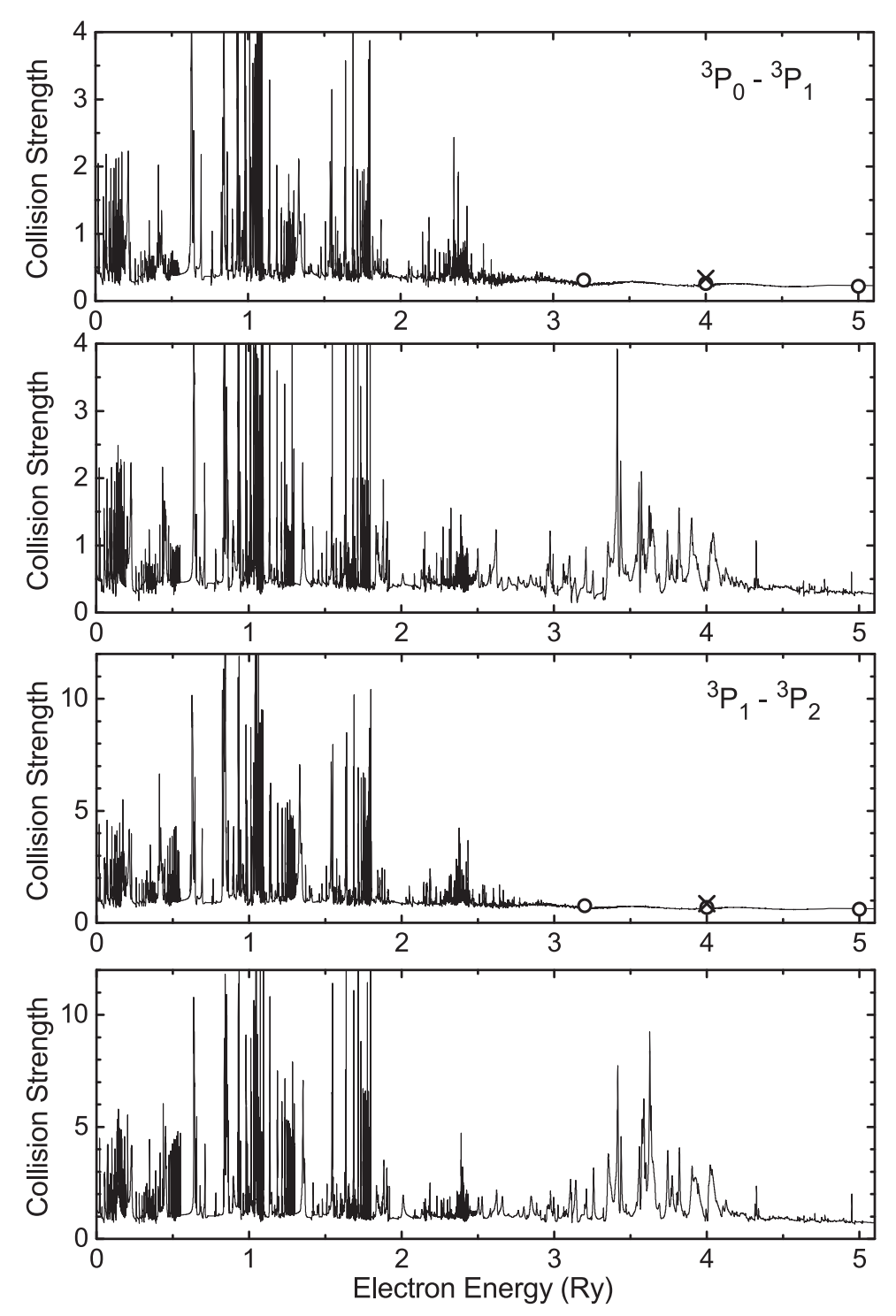


Figure 1. Collision strengths for the forbidden fine-structure $2p^2 {}^3P_0 - {}^3P_1$ and $2p^2 {}^3P_1 - {}^3P_2$ transitions are shown as a function of electron energy (in Ry). The first and third panels from the top show present results and second and fourth panels show the calculation of Palay et al. (2012) for the respective transitions. The *R*-matrix results of Aggarwal & Keenan (1999; open circles) and the distorted-wave calculation of Bhatia and Kastner (cross) are also shown in the nonresonant energy region.

fully relativistic MCDHF calculation of Jönsson & Bieroń (2010) shows a somewhat better agreement between the length and velocity results than the present calculation, which is probably because of the larger CI expansions used in their calculation. The additional configurations with smaller mixing coefficients in CI expansions normally impact the velocity values, while the length values normally remain stable. The good agreement with the MCDHF calculation of Jönsson & Bieroń (2010) indicates that the relativistic effects for O²⁺ are

not very important. Our length transition probabilities are in very good agreement with other theories for the stronger dipole-allowed transitions. The transition probabilities for the spin-changing intercombination transitions are small due to cancellation effects and display varied agreement with other theories. The transition probabilities for intercombination transitions are impacted by the size of CI expansions representing various types of correlation effects and interactions.

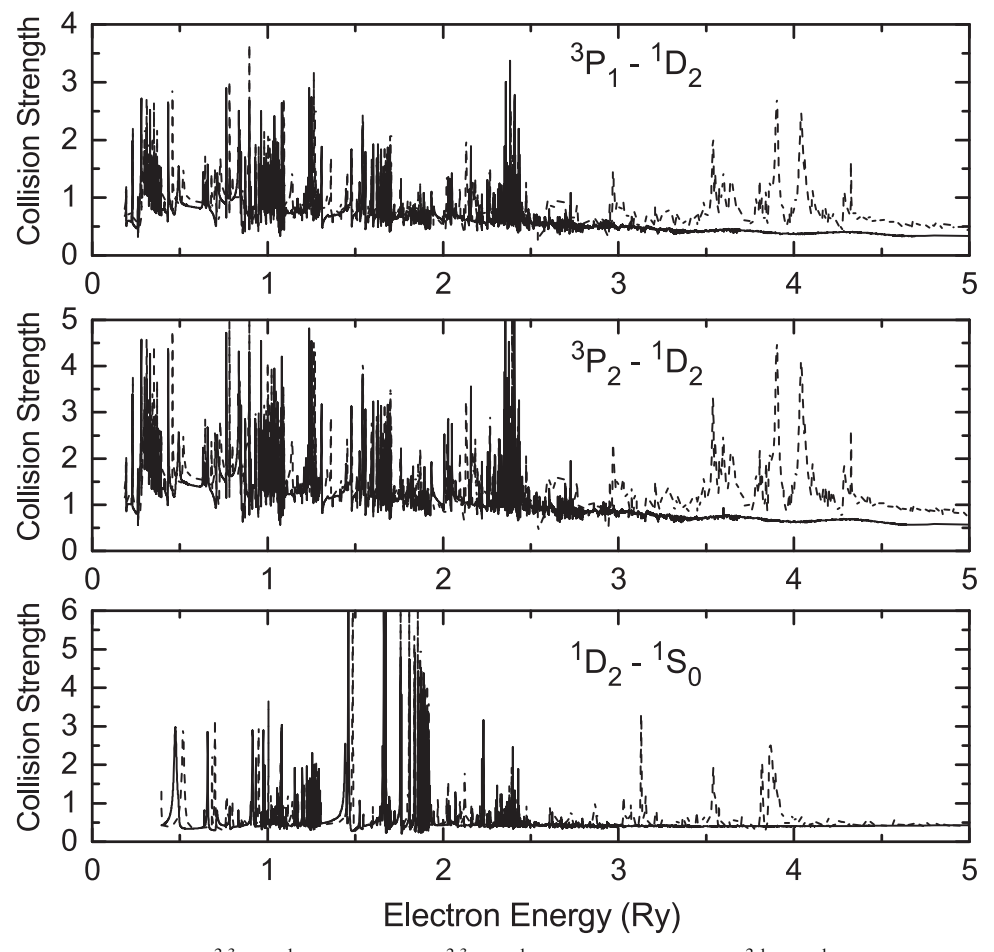


Figure 2. Collision strengths for the forbidden $2p^2 \, ^3P_1 - ^1D_2$ (top panel), $2p^2 \, ^3P_2 - ^1D_2$ (middle panel), and $2p^2 \, ^1D_2 - ^1S_0$ (bottom panel) transitions are shown as a function of electron energy (in Ry). The collision strengths from the present work are shown by solid curves and the results of Palay et al. (2012) are displayed by dashed curves.

The lifetimes of excited levels have been calculated from the E1, E2, M1, and M2 transition probabilities and have been given in Table 1 for all excited levels. Table 3 gives the present lifetimes of some lower levels and compares them with other calculations and measurements. The present lifetime for the $2s^22p^2$ 1S_0 level is in excellent agreement with the MCDHF calculation of Froese Fischer et al. (2009), heavy-ion storage ring measurement of Träbert et al. (2000), and the electron cyclotron ion source measurement of Smith et al. (2004). The theoretical value of Galavs et al. (1997) is about 7% higher than other calculations. The lifetime of the $2s2p^3$ ${}^5S_2^o$ level from the present work shows very good agreement with the MCHF calculation of Froese Fischer et al. (2009) and CIV3 calculation of Fleming & Brage (1997) and with the measurement of Johnson et al. (1984). The MCDHF calculation of Jönsson & Bieroń (2010) and multiconfiguration Dirac-Fock (MCDF; Grant et al. 1980) calculation of Fleming & Brage (1997) agree very well with each other, but are about 6% higher than the present result. The CIV3 result of Aggarwal et al. (1997) is somewhat larger than the other results. It is challenging to calculate accurate result for this level because of large cancellation between various configuration contributions. For other levels the present results are in excellent agreement with the calculations of Froese Fischer et al. (2009) and Luo et al. (1989). Our calculated values for these levels are also in agreement with the measured values of Pinnington et al.

(1974, 1978) within the uncertainties of the experiment. There is a reasonable agreement between the present calculation and the close-coupling calculation of Nahar (1998). The beam-foil measurement (Baudinet-Robinet et al. 1991) of lifetime for the $2s^22p3s$ $^1P_1^o$ level is significantly lower than the previous measurement of Pinnington et al. (1978) and all theories.

The length values of line strengths, oscillator strengths, and transition probabilities for E1, M1, E2, and M2 transitions between the fine-structure levels have been listed in Table 4. The first column gives the type of transition. The indices of initial and final levels of a transition are taken from Table 1 and are listed in columns 2 and 3. Column 4 gives the theoretical wavelengths in angstrom for the corresponding transitions. The line strength does not depend on calculated transition energy and the remaining error is due to the calculation of matrix elements. The intercombination transitions are usually much weaker than the allowed transitions. The intercombination lines are produced by the spin-orbit interaction due to mixing between different LS states with different (2S+1) values and the same set of quantum numbers J and π . The transition probabilities for the forbidden transitions are small and may be sensitive to CI and other effects. Normally, there is a good agreement between the present BSR plus MCHF results and previous MCHF calculations of Froese Fischer & Tachiev (2004) and Tachiev & Froese Fischer (2001). The form and contents of the data in

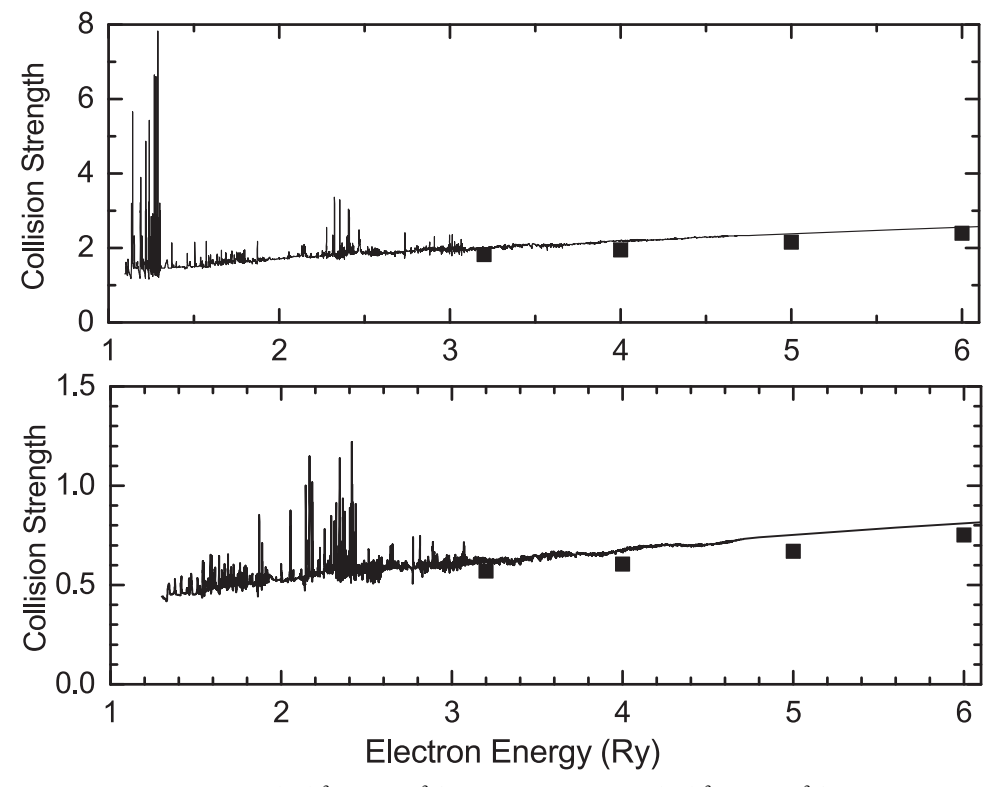


Figure 3. Collision strengths for the dipole-allowed $2s^22p^2$ $^3P_1 - 2s2p^3$ $^3D_2^o$ (upper panel) and $2s^22p^2$ $^3P_1 - 2s2p^3$ $^3P_1^o$ (lower panel) transitions are shown as a function of electron energy (in Ry). The *R*-matrix results of Aggarwal & Keenan (1999; solid rectangles) are also shown in the nonresonant energy region.

Table 4 are fully explained in the ReadMe files of the full machine-readable data files.

Total transition rates for the important optical lines at 5008 Å, 4960 Å, and 4933 Å have been compared in Table 5 with the previous most reliable results of Froese Fischer et al. (2009) and Storey & Zeippen (2000). These lines arise due to forbidden $2s^22p^2$ $^3P_{0,1,2}$ $^{-1}D_2$ transitions by magnetic dipole and electric quadrupole radiation and are observed in the spectra of gaseous nebulae. The lines at 5008 Å and 4960 Å arise due to both magnetic dipole and electric quadrupole radiation, but M1 transition rates dominate for these lines. On the other hand, the optical line at 4933 Å arises by E2 transition only and is much weaker than the other two lines, but there is still a very good agreement between the three calculations confirming the accuracy of results. As discussed by Froese Fischer et al. (2009) and Storey & Zeippen (2000), the relativistic corrections to the magnetic dipole transition operator can be important. Storey & Zeippen (2000) noted a 2%-4% increase in the transition rate for the $2s^22p^2$ $^3P_1 - ^1D_2$ transition in the considered C-like ions. Our results show very good agreement with the elaborate MCDHF II calculation of Froese Fischer et al. (2009) and Storey & Zeippen (2000). The line intensity ratios I(5008)/I(4960) and I(4933)/I(4960) have been shown in Table 6, where our results have been compared with the theoretical ratios from the works of Froese Fischer et al. (2009) and Storey & Zeippen (2000) and with the observed spectra of Orion Nebula (Baldwin et al. 2000; Esteban et al. 2004) and the Galactic H II region NGC 3576 (García-Rojas et al. 2006). The present I(5008)/I(4960) ratio agrees very well with the predicted values of Storey & Zeippen (2000) and MCHF and MCDHF calculations of Tachiev & Froese Fischer (2001) and Froese Fischer et al. (2009) respectively. Our calculation also shows good agreement with

observations, there is an especially excellent agreement with the measured value of García-Rojas et al. (2006). The intensity ratio I(4933)/I(4960) involves a much weaker line at 4933 Å. The predicted ratio from the present work is in reasonable agreement with other reliable calculations and is closer to the measured value of Baldwin et al. (2000).

3.2. Collision Data

Figure 1 displays collision strengths for the forbidden $2s^22p^2$ $^3P_0-2s^22p^2$ 3P_1 (upper two panels) and $2s^22p^2$ $^3P_1-2s^22p^2$ 3P_2 (lower two panels) transitions in the resonant energy region below the highest excitation threshold in our calculation and in a limited nonresonant energy region up to 5.1 Ry. The first and third panels from the top show present results and the second and fourth panels show the results of Palay et al. (2012). The collision strength shows rich resonance structures due to various Rydberg series of resonances converging to lower excitation thresholds. As a result, the resonance contributions are substantial in the energy region up to the $2s^22p3s$ $^1P_1^o$ threshold around 2.248 Ry. The accuracy of the target description is very good in our scattering calculation and therefore the resonances in the lower energy region should have correct positions. The resonances are very weak in the energy region of higher excitation thresholds in the present calculation. The comparison with the results of Palay et al. (2012) appears to be good up to about 2.5 Ry. However, the collision strengths from the calculation of Palay et al. (2012) contain resonances above 2.5 Ry, which seem to be pseudoresonances. In the energy region of all open channels, the collision strength varies smoothly with incident electron energy. The present results have been compared to the distorted-wave calculation of Bhatia & Kastner (1993) at 4.0 Ry and with the R-matrix calculation of Aggarwal & Keenan

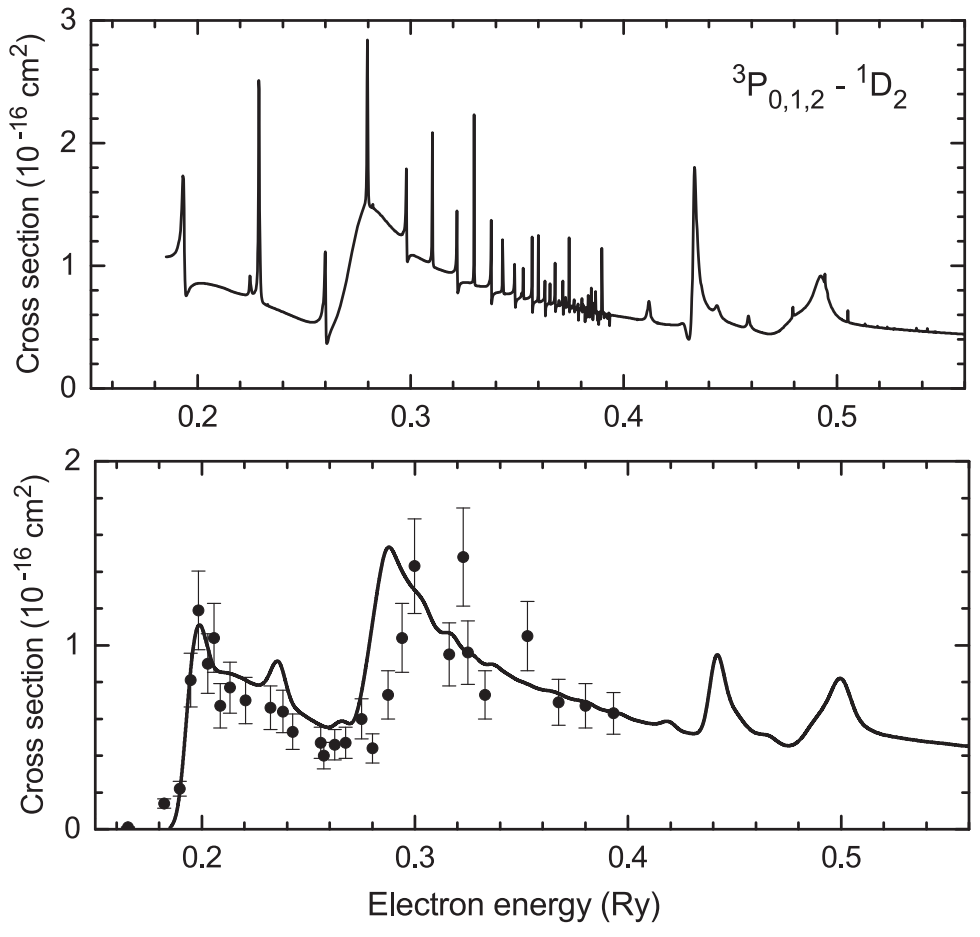


Figure 4. Combined cross sections for the $2s^22p^2$ $^3P_{0,1,2}$ $-2s^22p^2$ 1D_2 transitions shown as a function of electron energy in Ry. The upper panel shows the present cross sections prior to convolution and the lower panel shows the present convoluted results to the experimental energy spread of 0.00735 Ry. The experimental absolute cross sections (solid circles) with error bars are compared with the present convoluted results in the lower panel.

(1999) at 3.2, 4.0, and 5.0 Ry. Excellent agreement can be noted between the three calculations, indicating that there are no resonance contributions in this energy region. Aggarwal & Keenan (1999) transformed LS K-matrices from *R*-matrix calculation to LSJ coupling using algebraic recoupling scheme. Bhatia and Kastner presented distorted-wave calculation and ignored resonances from collision strengths.

Figure 2 gives the collision strengths for the $2s^22p^2$ $^1D_2 - 2s^22p^2$ 1S_0 (lower panel), $2s^22p^2$ $^3P_2 - 2s^22p^2$ 1D_2 (middle panel), and the $2s^22p^2$ $^3P_1 - 2s^22p^2$ 1D_2 transitions (top panel) in the energy region from threshold to 5.0 Ry. The present collision strengths have been displayed by solid curves and the results of Palay et al. (2012) have been shown by dashed curves. Generally, there is good agreement in the resonance structures at lower energies up to about 2.5 Ry with Palay et al. (2012). Again, the collision strengths from the calculation of Palay et al. (2012) appear to exhibit pseudo-resonances at energies above 2.5 Ry. There is also a shift in resonance positions to lower energies in the present calculation perhaps due to better representation of target states. We have plotted collision strengths for the allowed $2s^22p^2 {}^3P_1 - 2s2p^3 {}^3D_2^o$ and $2s^22p^2$ $^3P_1 - 2s2p^3$ $^3P_1^o$ transitions in Figure 3 as a function of electron energy from threshold to 6.1 Ry. The resonance structures are weaker for the allowed transitions than the forbidden transitions and the background collision strengths away from the resonances are larger. The collision strengths for

the allowed transitions exhibit increasing trend with electron energy. The collision strengths from the R-matrix calculation of Aggarwal & Keenan (1999) are also shown at 3.2, 4.0, 5.0, and 6.0 Ry. The present results are slightly larger than the calculation of Aggarwal & Keenan (1999).

The electron energy-loss merged electron and ion beam measurements are available for the combined optical lines at wavelengths 5009.0 Å and 4960.0 Å (Niimura et al. 2002). They reported absolute direct combined excitation cross sections for the forbidden $2s^22p^2$ $^3P_{0,1,2}-2s^22p^2$ 1D_2 transitions in the energy range from threshold at 0.182 Ry to 0.393 Ry and compared measured cross sections with the R-matrix calculation of Aggarwal & Keenan (1999). We have plotted our combined cross section for the $2s^22p^2$ $^3P_{0,1,2} - 2s^22p^2$ 1D_2 transitions in the upper panel of Figure 4. In order to compare our results with the experiment, we convoluted the calculated cross sections to the energy resolution of 0.00735 Ry in the experiment. The convoluted theoretical cross sections have been compared in the lower panel of Figure 4. The uncertainty in the measured cross sections has been reported to be about 18%, and it is displayed by error bars. Our convoluted cross sections are within the experimental error bars for many energies and outside the error bars for some other energies. There is excellent agreement between theory and experiment for the first peak in cross section around 0.198 Ry. The second peak around 0.228 Ry predicted by our calculation as well as

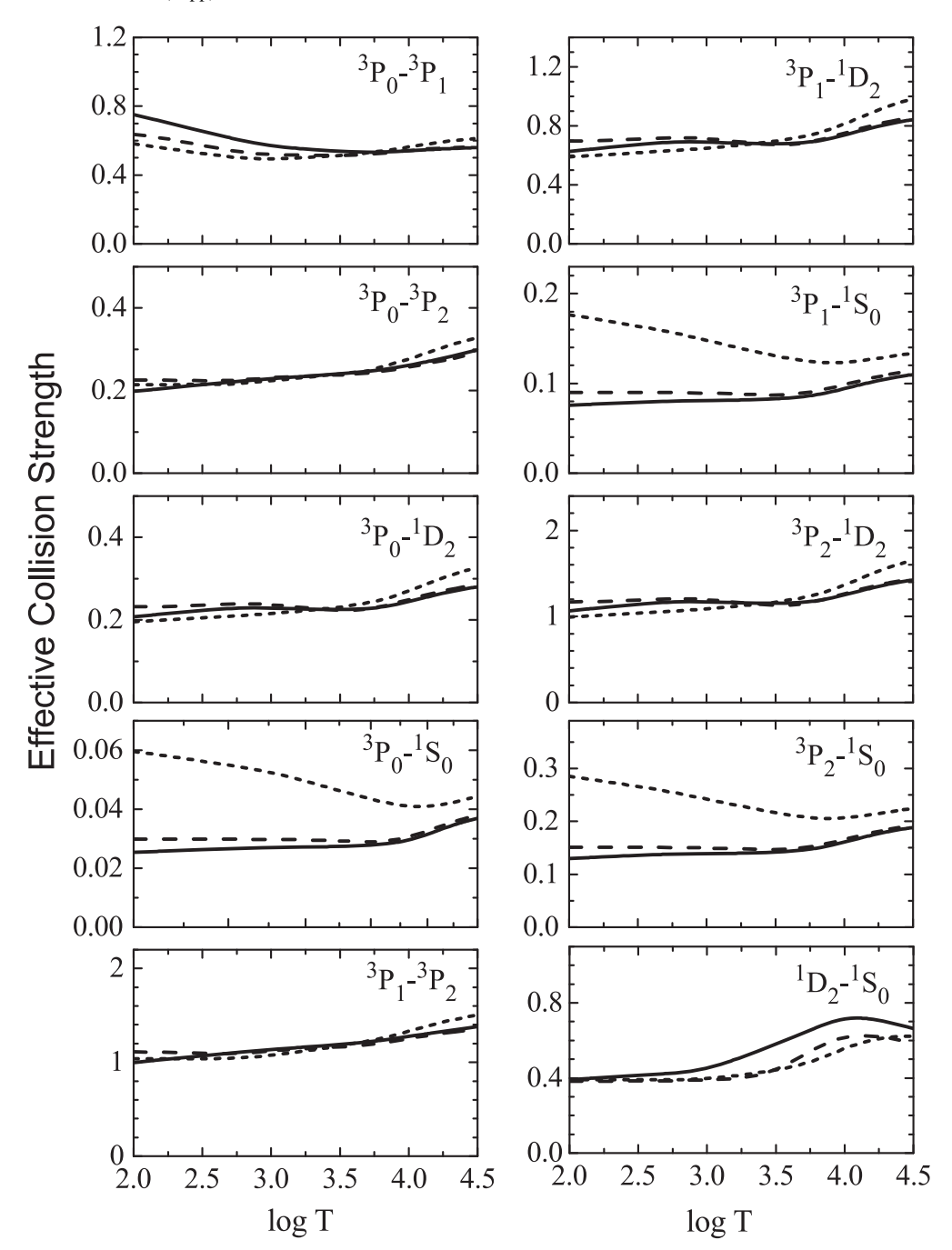


Figure 5. Comparison of present thermally averaged collision strengths (solid curve) with the BPRM calculations of Palay et al. (2012; short-dashed curve) and Storey et al. (2014; long-dashed curve) for transitions between the lowest five fine-structure levels of the $2s^22p^2$ ground configuration as a function of electron temperature.

by Aggarwal & Keenan (1999) is not detected by the experiment. The third broad peak around 0.294 Ry is present in both calculations and the experiment. However, it appears to be broader in both theories and shifted to lower energy in our calculation. It may be noted that our threshold energies are in better agreement with the experiment than those of Aggarwal & Keenan (1999). The cause of disagreement in the position of third peak is not clear and further work is needed.

Thermally averaged collision strengths for 10 transitions between the lowest five levels of the ground $2s^22p^2$ configuration have been shown in Figure 5 as a function of electron temperature from log T=2.0 to 4.5. The present

results (solid curve) have been compared with the BPRM calculations of Storey et al. (2014; long-dashed curve) and Palay et al. (2012; short-dashed curve). There is an overall good agreement between the present calculation and that of Storey et al. (2014). Noticeable differences with the calculation of Storey et al. (2014) can be noted only at lower temperatures and the results from two calculations converge to each other except for the $2s^22p^2$ 1D_2 - $2s^22p^2$ 1S_0 transition. For this transition, our results compare very well at lower temperatures, but differ significantly at temperatures log $T \gtrsim 3.0$. Both calculations exhibit a peak in thermally averaged collision strengths around log T = 4.0. There

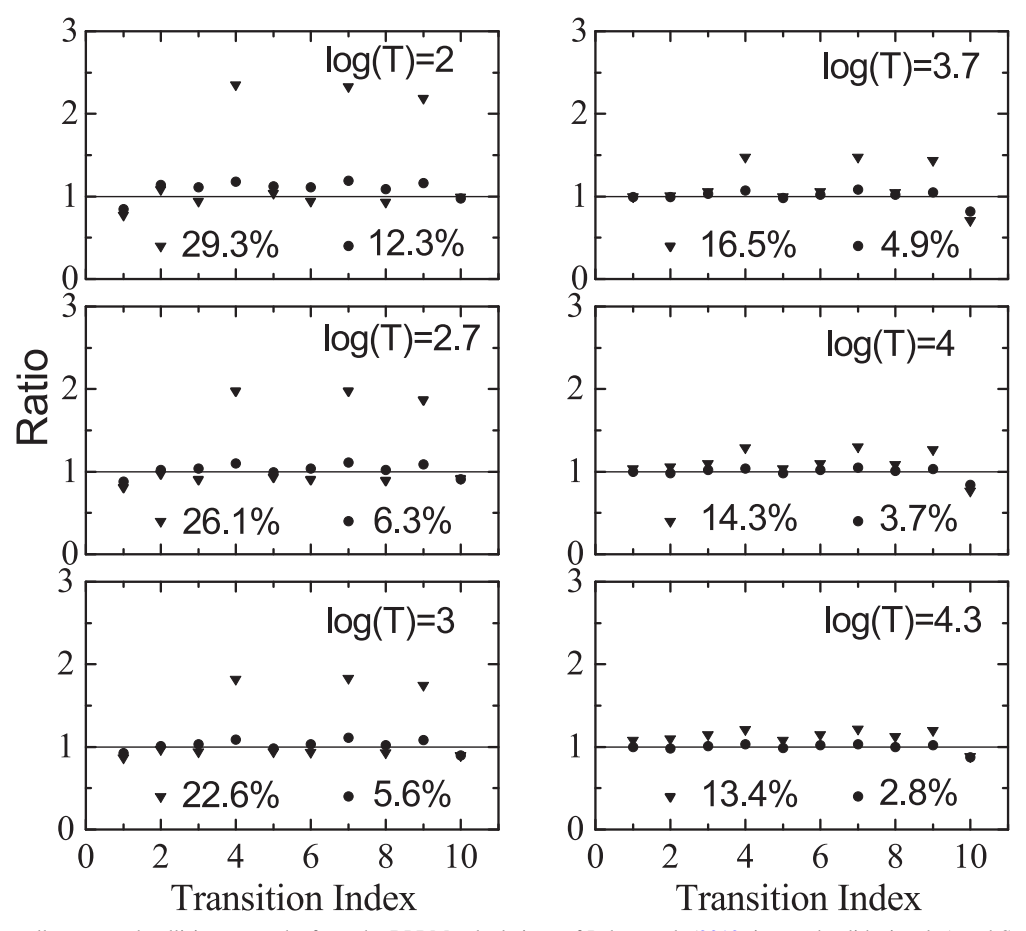


Figure 6. Ratio of thermally averaged collision strengths from the BPRM calculations of Palay et al. (2012; inverted solid triangles) and Storey et al. (2014; solid circles) with the present results for 10 transitions between the fine-structure levels of the $2s^22p^2$ ground configuration at electron temperatures from log T=2.0 to 4.3. The percentage indicates the average difference with other results.

are larger discrepancies with the calculation of Palay et al. (2012), especially for transitions involving the $2s^22p^2$ 1S_0 level. They used a modified version of the BPRM code that included two-body Breit interaction terms. The relativistic effects for the O²⁺ ion are small, and it seems unlikely that the additional two-body relativistic effects can cause these discrepancies. The ratios of thermally averaged collision strengths from the BPRM calculations of Palay et al. (2012) and Storey et al. (2014) with the present results for 10 transitions between the fine-structure levels of the $2s^22p^2$ ground configuration have been plotted in Figure 6 at six electron temperatures from $\log T = 2.0$ to 4.3. The present results show the largest differences with other calculations at $\log T = 2.0$; 29.3% with Palay et al. (2012) and 12.3% with Storey et al. (2014). The agreement improves with increasing temperature and the discrepancies between the present results and those of Palay et al. and Storey et al. are 13.4% and 2.8%, respectively, at log T = 4.3. The largest discrepancies for Palay et al. occur for the transitions involving the $2s^22p^2$ 1S_0 level. The ratio of thermally averaged collision strengths from the R-matrix calculations of Aggarwal & Keenan (1999) with present results for transitions between the lowest 49 fine-structure levels of the $2s^22p^2$, $2s2p^3$, $2p^4$, and $2s^22p3l$ (l = 0-2) configurations have been shown in Figure 7 at 10 electron temperatures from 2500 K to 200,000 K. The percentage agreement within the 50%

tolerance is also shown at different temperatures. The two calculations agree to within 50% only for less than half of the transitions. The agreement appears to be better for the stronger transitions and the agreement for highly excited states is more diverse. We have attempted to obtain a highly accurate target description and accounted for important physical effects. The Rydberg series of resonances converging to several excited levels are found to enhance collision strengths substantially. We have included relativistic effects in the BPRM approach directly and we used extensive CI expansions for the description of target levels, which may be contributing to some of the differences.

We have listed in Table 7 thermally averaged collision strengths for all inelastic transitions between 202 fine-structure levels considered in the present calculations giving rise to a total of 20,301 transitions. The results are given at 10 temperatures covering a broad range of 100, 500, 1000, 5000, 10,000, 20,000, 40,000, 60,000, 80,000, and 100,000 K. These results cover infrared, optical, and ultraviolet emission lines for modeling of various types of astrophysical plasmas. The keys of the lower and upper levels of transitions have been taken from Table 1. The thermally averaged collision strengths exhibit expected behavior at higher temperatures for the allowed, intercombination, and forbidden transitions. The relativistic effects appear to be small, especially for lower excited levels. The entire contents of Table 7 have been

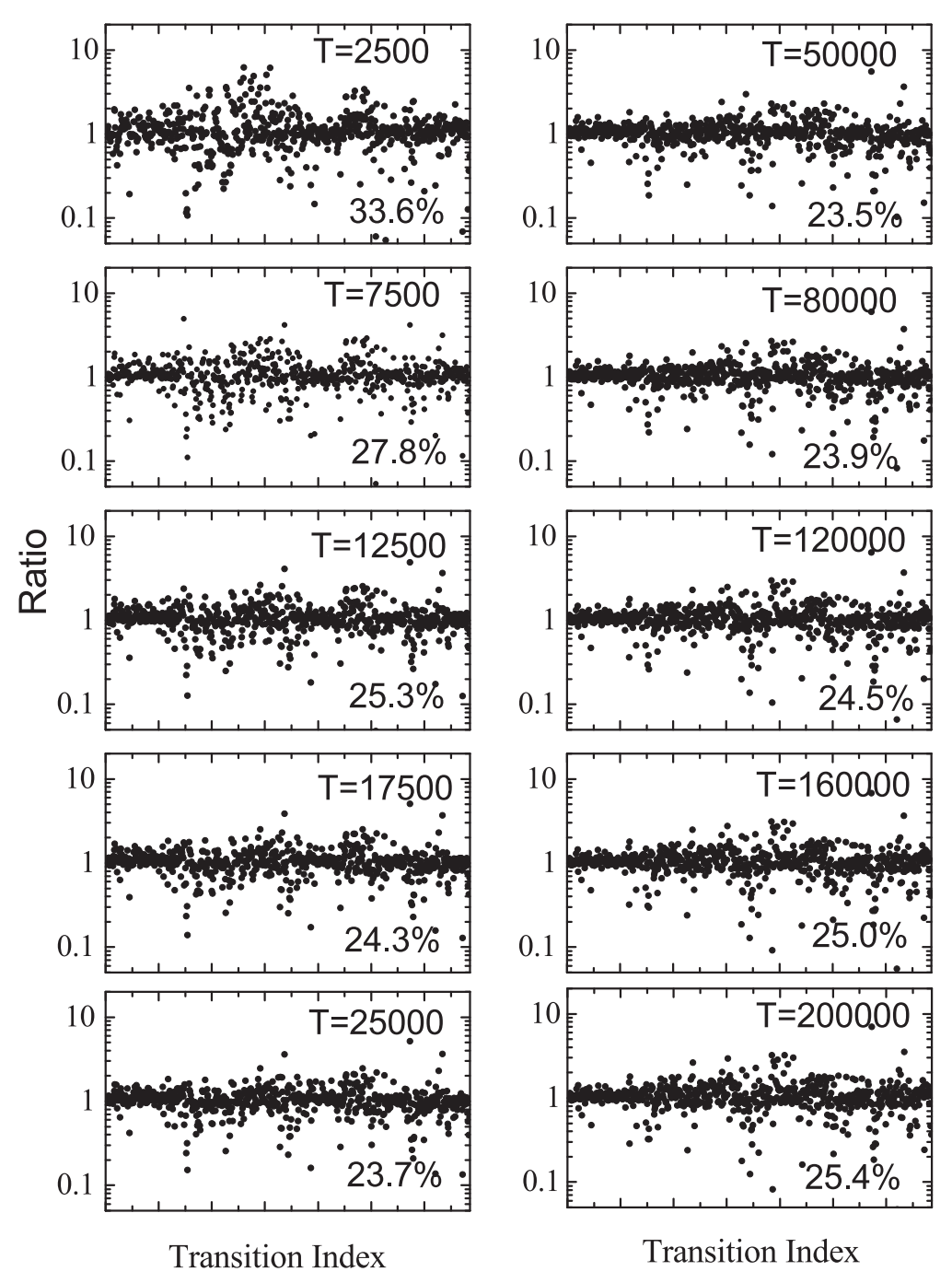


Figure 7. Ratio of thermally averaged collision strengths from the *R*-matrix calculations of Aggarwal & Keenan (1999) with the present results for transitions between the lowest 49 fine-structure levels of the $2s^22p^2$, $2s2p^3$, $2p^4$, and $2s^22p31$ (l=0-2) configurations at 10 electron temperatures from 2500 K to 200,000 K. The percentage agreement within the 50% is also given.

published in a machine-readable format with an associated ReadMe file.

4. Summary

We have presented thermally averaged collision strengths and radiative parameters for all transitions among the lower 202 fine-structure levels of O^{2+} . The present results are most extensive and considerably expand the existing data sets for O^{2+} , allowing more detailed treatment of the available measured spectra from different ground and space observatories. The calculations were performed with the advanced BSR

code (Zatsarinny 2006), which employs the BPRM method in the B-spline basis. To represent the target states, we used term-dependent orbital sets, which allowed us to generate a more accurate description of the O^{2+} target states than those employed before in other calculations. Both short-range and long-range correlation effects in the target states have been included accurately. The calculated excitation energies show excellent agreement with the available experimental values for most levels considered in our work. We have presented a detailed comparison of transition probabilities and lifetimes of excited levels to assess the accuracy of radiative data for O^{2+} . The line intensity ratios for the astrophysically important

 Table 7

 Effective Collision Strengths for Fine-structure Transitions in O III

i–k					$T \times$	10^{3} K				
	0.1	0.5	1.0	5.0	10.0	20.0	40.0	60.0	80.0	100.0
1 2	7.52E-01	6.17E-01	5.62E-01	5.25E-01	5.42E-01	5.56E-01	5.63E-01	5.69E-01	5.69E-01	5.66E-01
1 3	1.98E-01	2.21E-01	2.30E-01	2.45E-01	2.61E-01	2.82E-01	3.07E-01	3.23E-01	3.31E-01	3.34E-01
1 4	2.08E-01	2.30E-01	2.29E-01	2.21E-01	2.44E-01	2.70E-01	2.86E-01	2.89E-01	2.87E-01	2.83E-01
1 5	2.54E-02	2.71E-02	2.72E-02	2.77E-02	3.15E-02	3.53E-02	3.77E-02	3.81E-02	3.80E-02	3.76E-02
1 6	7.95E-02	8.75E-02	8.82E-02	9.96E-02	1.11E-01	1.18E-01	1.17E-01	1.13E-01	1.07E-01	1.03E-01
1 7	1.44E-02	2.58E-02	3.34E-02	7.77E-02	8.98E-02	8.48E-02	6.78E-02	5.69E-02	4.96E-02	4.44E-02
1 8	4.92E-02	6.01E-02	6.57E-02	8.31E-02	8.81E-02	8.69E-02	8.04E-02	7.58E-02	7.25E-02	6.99E-02
19	5.14E-01	5.79E-01	6.07E-01	6.34E-01	6.41E-01	6.47E-01	6.59E-01	6.74E-01	6.90E-01	7.05E-01
1 10	2.20E-02	2.44E-02	2.58E-02	3.31E-02	3.18E-02	2.98E-02	2.81E-02	2.72E-02	2.64E-02	2.56E-02
1 11	4.51E-01	4.88E-01	4.90E-01	4.93E-01	5.04E-01	5.21E-01	5.46E-01	5.67E-01	5.86E-01	6.03E-01

(This table is available in its entirety in machine-readable form.)

optical lines have been presented. A very good agreement with previous calculations and observations confirms the reliability of the radiative data to some extent. The accuracy of the available collision data for lower astrophysically important transitions has been assessed by comparison with other calculations and experiment. There is an overall good agreement between the calculated and measured cross sections for the combined $2s^22p^2$ $^3P_{0,1,2} - 2s^22p^2$ 1D_2 transitions. The present calculation agrees better with the work of Storey et al. (2014) than the calculation of Palay et al. (2012), especially for transitions involving $2s^22p^2$ 1S_0 level. The effective collision strengths are presented over a wide range of temperatures and should be useful for the modeling of astrophysical plasmas.

This work was supported by the United States National Science Foundation under grant No. 1714159 from the Astronomy and Astrophysics Program.

ORCID iDs

S. S. Tayal https://orcid.org/0000-0003-1805-0930

References

```
Aggarwal, K. M., Hibbert, A., & Keenan, F. P. 1997, ApJS, 108, 393
Aggarwal, K. M., & Keenan, F. P. 1999, ApJS, 123, 311
Badnell, N. R. 1999, JPhB, 32, 5583
Badnell, N. R. 2011, CoPhC, 182, 1528
Baldwin, J., Verner, E. M., Verner, D. A., et al. 2000, ApJS, 129, 229
Baudinet-Robinet, Y., Dumont, P. D., & Garnir, H. P. 1991, PhRvA, 43, 4022
Berrington, K. A., Eissner, W. B., & Norrington, P. H. 1995, CoPhC, 92, 290
Bhatia, A. K., & Kastner, S. O. 1993, ADNDT, 54, 133
Binette, L., Matadamas, R., Hagele, G. F., et al. 2012, A&A, 547, A29
Delamere, P. A., Bagenal, F., & Steffl, A. 2005, JGR, 110, A12223
Doschek, G. A., Mariska, J. T., & Akiyama, S. 2004, ApJ, 609, 1153
Esteban, C., Peimbert, M., García-Rojas, J., et al. 2004, MNRAS, 355, 229
Fleming, J., & Brage, T. 1997, JPhB, 30, 1385
Froese Fischer, C. 2007, CoPhC, 176, 559
Froese Fischer, C., & Tachiev, G. 2004, ADNDT, 87, 1
```

```
Froese Fischer, C., Tachiev, G., Rubin, R. H., & Rodríguez, M. 2009, ApJ,
Galavs, M. E., Mendoza, C., & Zeippen, C. J. 1997, A&AS, 123, 159
García-Rojas, J., Esteban, C., Peimbert, M., et al. 2006, ApJS, 153, 501
Grant, I. P., McKenzie, B. J., Norrington, P. H., & Mayers, D. F. 1980, CoPhC,
Hibbert, A. 1975, CoPhC, 9, 141
Johnson, C., Smith, P., & Knight, R. D. 1984, ApJ, 281, 477
Jönsson, P., & Bieroń, J. 2010, JPhB, 43, 074023
Jönsson, P., He, X., Froese Fischer, C., & Grant, I. P. 2007, CoPhC, 177,
Kramida, A. E., Ralchenko, Yu., Reader, J. & NIST ASD Team 2013, NIST
   Atomic Spectra Database (Gaithersburg, MD: National Institute of
  Standards and Technology), http://physics.nist.gov/asd3
Lennon, D. J., & Burke, V. M. 1994, A&AS, 103, 273
Luo, D., Pradhan, A. K., Saraph, H. E., Storey, P. J., & Yu, Y. 1989, JPhB,
   22, 389
Maiolino, R., Nagao, T., Grazian, A., et al. 2008, A&A, 488, 463
Mendoza, C., & Bautista, M. A. 2014, ApJ, 785, 91
Nahar, S. N. 1998, PhRvA, 58, 3766
Nicholls, D. C., Dopita, M. A., Sutherland, R. S., Kewley, L. J., & Palay, E.
  2013, ApJS, 207, 21
Niimura, M, Smith, S. J., & Chutjian, A. 2002, ApJ, 565, 645
Palay, E., Nahar, S. N., Pradhan, A. K., & Eissner, W. 2012, MNRAS,
Pinnington, E. H., Donnelly, K. E., & Irwin, D. J. G. 1978, CaJPh, 56, 508
Pinnington, E. H., Irwin, D. J. G., Livingston, A. E., & Kernahan, J. A. 1974,
  CaJPh. 52, 1961
Rubin, R. H., Martin, P. G., Dufour, R. J., et al. 2003, MNRAS, 340,
Smith, S. J., Cadez, I., Chutjian, A., & Niimura, M. 2004, ApJ, 402, 1075
Spinoglio, L., Pereira-Santaella, M., Dasyra, K. M., Calzoletti, L., et al. 2015,
   ApJ, 799, 21
Steffl, A., Bagenal, F., & Stewart, A. I. F., 2004a, Icar, 172, 91
Steffl, A., Stewart, A. I. F., & Bagenal, F. 2004b, Icar, 172, 78
Storey, P. J., & Sochi, T. 2015, MNRAS, 449, 2974
Storey, P. J., Sochi, T., & Badnell, N. R. 2014, MNRAS, 441, 3028
Storey, P. J., & Zeippen, C. J. 2000, MNRAS, 312, 813
Tachiev, G., & Froese Fischer, C. 2001, CaJPh, 79, 955
Tayal, S. S., & Zatsarinny, O. 2011, ApJ, 743, 206
Tayal, S. S., & Zatsarinny, O. 2014, ApJ, 788, 24
Träbert, E., Calamai, A. G., Gillaspy, J. D., et al. 2000, PhRvA, 62, 022507
Zatsarinny, O. 2006, CoPhC, 174, 273
Zatsarinny, O., & Froese Fischer, C. 2009, CoPhC, 180, 2041
```